NTNU – Trondheim
Norwegian University of
Science and Technology

Nano-Indentation of Anisotropic Material: Numerical Approaches to Extract Elasticities from Nano-Indentation

Tore Sveaass

Master of Science in Mechanical Engineering
Submission date: June 2013
Supervisor: Bjørn Helge Skallerud, KT

Norwegian University of Science and Technology
Department of Structural Engineering

Abstract

Master of Science

Nano-indentation of anisotropic material: numerical approaches to extract elasticities from nano-indentation

by Tore Sveaass

Division of Biomechanics participates in a project together with Department of Cancer Research and Molecular Medicine, NTNU, on effects of proton pump inhibitor medication on bone quality. This common anti-stomach acid medication seems to result in an increased bone fragility in humans. As a step towards comparing mechanical properties at micro level, between sick and healthy bone tissue, mice femur have been tested at micro level using the increasingly popular tool, nanoindentation. Futher, an analytical finite element model has been created in an effort to increase the understanding of nanoindentation of bone. It is concluded that the experimental protocol is not accurate enough(SD $\approx$ 5GPa for reduced Young's modulus) as a result of multiple factors, mainly indentation locations. The experimental results were compared to the finite element model. It was possible to match the data curves of the experimental tests with the analytical tests by adjusting the model parameters. Unfortunatly, this resulted in divergent results($\sigma_Y \approx$ 600MPa and reduced Young's modulus of nearly 60% of the experimental data(32,45 GPa and 20GPa). As an effort to reduce the divergence between the experimental and analytical testing, multiple suggestions were made.

Abstrakt

Master of Science

Nanoindentering av anisotropisk materiale: numerisk tilnærming for å hente ut elastisiteter gjennom nanoindentering

av Tore Sveaass

Biomekanisk avdeling ved institutt for konstruksjonsteknikk ved NTNU deltar i et samarbeidsprosjekt med avdeling for kreftforskning og molekulær medisin ved NTNU om å vurdere effektene ved behandling med protonpumpehemmer(PPI). PPI ser ut til å fremme benskjørhet hos mennesker.

For å sammenlikne syke og friske bens mekaniske egenskaper på mikronivå har museben blitt testet gjennom nanoindentering - en teknikk som stadig øker i popularitet. Videre er det blitt laget en elementmodell i et forsøk på å øke forståelsen rundt nanoindentering av ben. Det konkluderes at de eksperimentelle forsøkene ikke utføres nøyaktig nok (SD $\approx$ 56GPa for redusert elastisk modulus) som følge av mange faktorer; hovedsakelig indenteringens lokasjon på benet. De eksperimentelle resultatene ble sammenliknet med de analytiske. Det var mulig å justere parameterene i den analytiske modellen slik at datakurven fulgte de eksperimentelle perfekt. Dessverre var dette kun mulig med motstridene resultater. σ_Y ble anslått til å være $\approx$ 600MPa og den reduserte elastiske modulusen måtte reduseres til 60% av den eksperimentelle modulusen(20GPa mot 32,45GPa).Det er blitt foreslått mange forbedringer for at de eksperimentelle resultatene skal bli mer nøyaktige, og for at de analytiske skal bli mer troverdige.

Acknowledgements

This thesis is the final work concluding my Mechanical Engineering study at the Norwegian University of Science and Technology, NTNU. A major part of the thesis is numerical analyses carried out with the finite element program ABAQUS/-CAE. The work has been conducted at the Department of Structural Engineering.

I want to thank my supervisor Professor Bjørn Helge Skallerud, Ph.D. candidate Masoud Ramezanzadehkoldeh and Associate Professor Jianying He for all the help and support during this final semester. The informal correspondance and meetings have been essential for my master thesis.

I also want to thank my family and friends for supporting me throughout the whole study.

Contents

List of Figures

List of Tables

Abbreviations

SD	**Standard Deviation**
VE	**Visco Elastic**
VEP	**Visco Elastic Plastic**
ECM	**Extra Cellular Matrix**
BNH	**Brinell Hardness**
DPH	**Diamond Pyramid Hardness**
FEM	**Finite Element Method**
RCF	**Ramp Correction Factor**
SE	**Standard Error**
AFM	**Atomic Force Microscop**

Physical Constants

Young's modulus for diamond	E_i	=	1141GPa
Poisson's ratio for diamond	ν_i	=	0,07

Symbols

H	Contact hardness, resistance to total deformation
H_C	Contact hardness
d	Diameter for area when sphere is in contact with surface
C_i	creep function coefficients
D	Diameter for the sphere in contact with surface
f	Viscous extent ($\frac{G_\infty}{G_0}$)
G	Shear modulus
G_0	Zero-time shear modulus
G_∞	equilibrium shear modulus
G^I	incompressible shear modulus
P	Load
P_{max}	Peak load
m	Material parameter
h	Indentation displacement
h_e	Elastic displacement
h_f	Final indentation displacement
h_c	Contact displacement
h_{max}	Maximum displacement
h_p	Plastic displacement
h_v	Viscous displacement
E^*	Reduced elastic modulus/Indentation modulus
$E^{'}$	Plain strain modulus
A	Indentation area

A_c	Contact area
t	Time
t_C	Creep hold time
t_R	Rise time
S	Stiffness
n_Q	Indentation viscosity
RCF	Accounts for non instantaneous loading

μ_x	Mean value
σ_x	Standard deviation
σ_{Mises}	Von Mises yield criteria
σ_Y	Yield stress
ϵ_i	Effective indentation strain
α	Material parameter
$\alpha_1, \alpha_2, \alpha_3$	Dimensionless geometry constant
β	Correction factor for pyramidal geometries
ν	Poisson's ratio
τ_i	viscouselastic time constant

Chapter 1

Introduction and background

1.1 Background

Division of Biomechanics participates in a project together with Deparment of Cancer Research and Molecular Medicine, NTNU, on effects of proton pump inhibitor medication on bone quality. This common anti-stomach acid medication seems to result in an increased bone fragility in humans. The project uses mouse as animal model, with different groups subject to different genetic modifications and medications (including controls) to study the stiffness and strength of the femur bone quality. Three- point bend tests are carried out to assess effects of medication on global response of the femur. This is a part of MSc Masoud Ramezanzadekoldeh PhD project. Pieces from the three point bending tests will be fixed in resin and employed in nanoindentation tests. This will further provide information of local stiffness relative to the global stiffness measure in three point bend.

1.2 Scope

The project addresses both experiments and numerical simulation of nanoindentation of mouse femur. An experimental protocol is defined (locations and number of indentations per location). Finite element simulations are carried out accordingly.

The boundary effect of the bone embedded in resin should be investigated. Several approaches to material modeling of the bone can be investigated, e.g. isotropic elasto-plastic material, transversely isotropic or orthotropic, and feasibility of axi-symmetric versus 3D models should be addressed. The indentation stiffness from experiments and simulation is compared and the FEA modeling discussed. Finally, the correspondence(or lack of correspondence) between measured elasticity and global stiffness found in three point bend tests on same material is discussed.

Chapter 2

Background

2.1 Bone

The skeletal system provides protection for vital organs, transforms energy from muscles to movement, forms blood and operates as a reservoir for minerals that contribute to homeostatic regulations. [1] [2]. Bone should be tough, and stiff, however those properties run contrary to each other [3]. Currey has dived the structure of bone into four levels of hierarchy, from bottom-up: Nanoscale, microscale, mesoscale and the whole bone scale, see figure 2.1.

A brief presentation of these four levels will now be presented.

2.1.1 Whole bone and mesoscale - The human femur

Figure 2.2 shows the human femur where the head and neck is connected to the pelvis on the top and the knee joint at the bottom. At mesoscale, it is normal to devide the bone into three parts (figure 2.3) epiphysis, metaphysis and diaphysis, and the macroscopic bone types into spongy and compact bone.

The spongy bone(trabecular, cancellous) and compact bone(cortical) are seen in the cavity and at the periphery of the bone, respectively. In adults, the ratio of

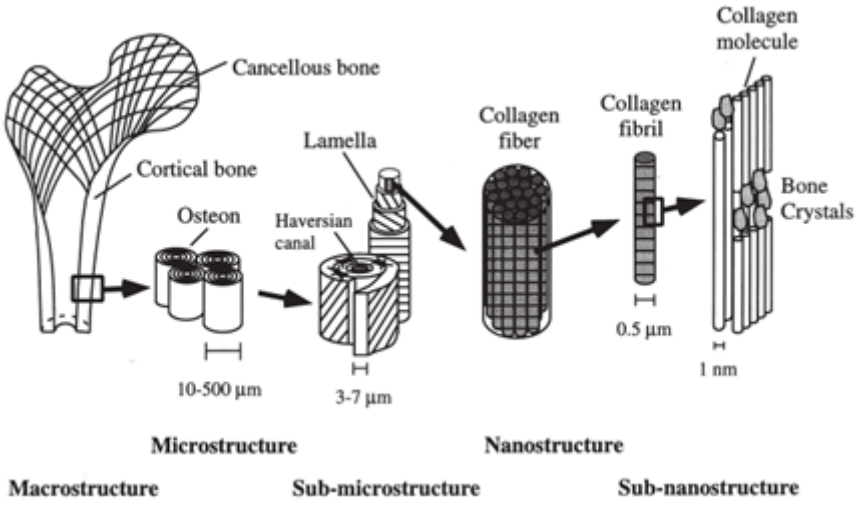

FIGURE 2.1: A simple illustration of different levels of the bone, borrowed from Rho et al. [4]

FIGURE 2.2: Human femur, taken from [4]

cortical bone to trabecular bone typically is 80:20 [2]. The diaphysis, the middle part of long bones, has a thick part of cortical bone and is extremely strong. Therefore, it does not require a large diameter to carry its load [2]. Cancellous bone on the other hand is seen to dominate at the end of long bones, and this bonetype has a damping effect on impacts from other joints.

It is difficult to analyze the material properties of cancellous bones because it is partway from being a structure and one might ask if the material properties are the same as those of compact bone. [1]

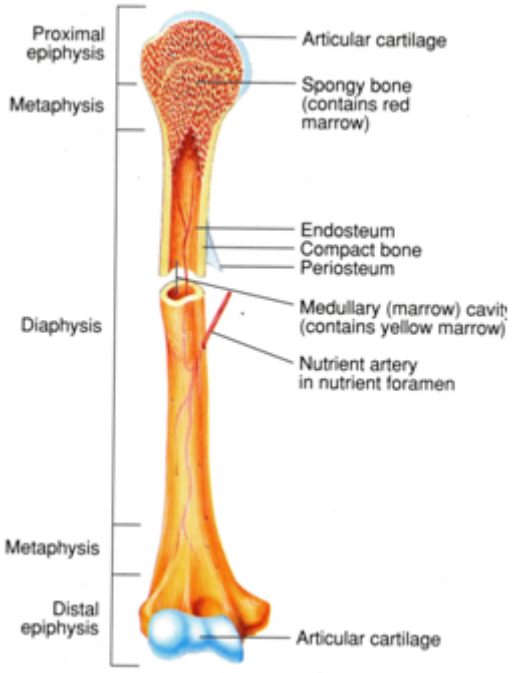

FIGURE 2.3: The human femure divided: epiphysis, metaphysis and diaphysis of the femur, from [5]

2.1.2 Bones at microscale

Bone tissue, based on matrix arrangement can be classified as lamellar bone, woven bone or haversian (secondary) bone, named after Clopton Havers(b. 1657). Mature cortical bone is lamellar, meaning it has a distinct layered structure [2]. The primary unit of the bone is called an osteon. An osteon is a cylindershaped network of bone that is centered and surrounding a vascular canal called the haversian canal. In contrast to sponge bone, where the lamellae are arranged parallel to each other, in compact bone, the lamellae are arranged concentrically around the haversian canal. Figure 2.4 illustrates this structure.

Woven bone(figure 2.5 is immature bone, in which lamellae are arranged in irregular random arrays and contains smaller amounts of mineral substance and a higher proportion of osteocytes than lamellar bone. Woven bone is temporary and is eventually converted to lamellar bone [1]. It is disorganized bone, created through random organization of collagen and minerals. It probably has, though this is not known for certain, poor mechanical properties [3].

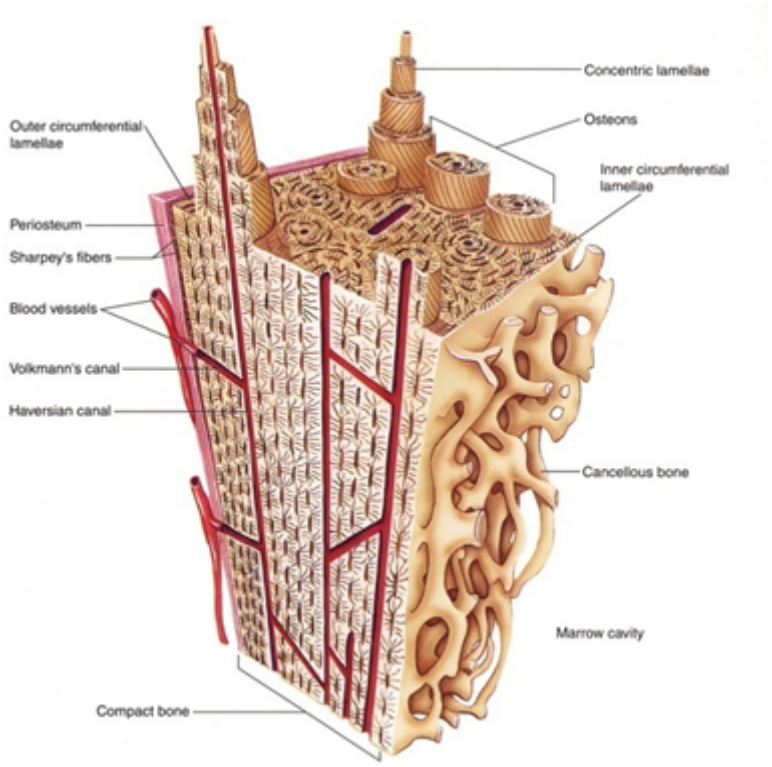

FIGURE 2.4: The haversian canal, osteons and lamellae are illustrated [6]

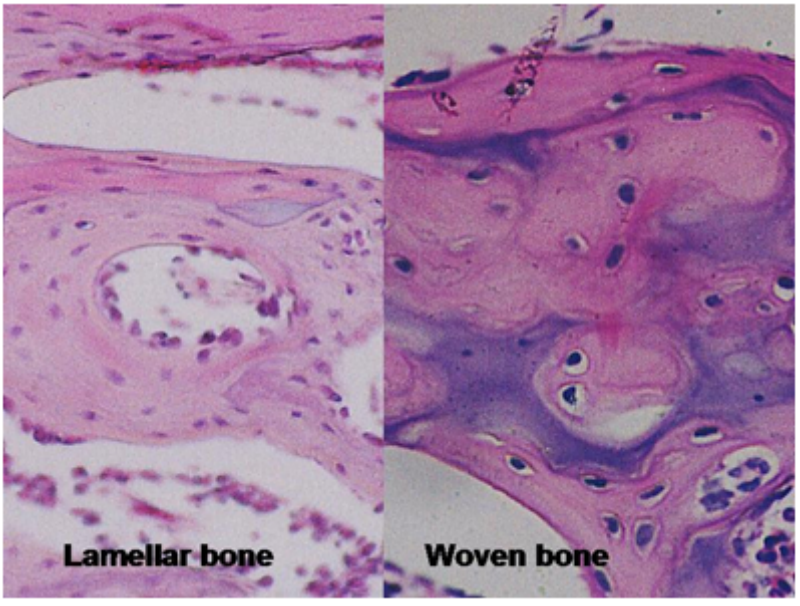

FIGURE 2.5: "Histological cut showing details of lamellar bone concentrically organized and woven bone mixed with cartilage and calcified cartilage tissues (HE)" [7]

2.1.3 Nanoscale

Bone as a whole has a low cell content and is made primarily of noncellular matrices. There are two forms of extracellular matrix (ECM): osteoid and mineralized matrix,. Osteoid is immature matrix excreted by osteoblasts. It is then converted to mature mineralized matrix over time. Bone matrix consists of mineral, proteins (collagen), glycoprotein, proteoglycans and water [2]. Osteoid is made by osteoblasts and is found in areas of new bone formation. Osteoid is mostly proteinaceous. Type I collagen is by far the most important of the numerous collagens in the human body. It forms a triple helical structure that is en then condensed and elongated into fibrils. Because of this unique arrangement of chains and the importance of proline in the formation of chains, type I collagen forms one of the longest, thinnest and most rigid protein structures. Hole zone regularly found in the collagen fibrils allow attachement of mineral crystals. [2] Extracellular matrix is largely $60 - 70\%$ mineral. The principal minerals involved are calcium and phosphate. The remainder of the ECM os protein 25% and water. The protein of the bone is dominated by type I collagen (90%). The ECM gives the bone it mechanical properties. [2]

2.1.4 Comments

A brief introduction to the different levels has been made, and one can see how complex the bone material becomes as the scale decreases. To understand interplay between the structural units on different levels, methods have been created, and experiments have been done. One of the techniques is introduced in the next part.

2.2 Nanoindentation

2.2.1 Introduction

The idea behind nanoindentation builds upon work from the late 19th century done by Hertz on contact mechanics [8]. Hertz studied the effect of two spheres in contact(figure 2.6) and developed an elastic theory of contact based on the stresses of two elastic solids. His analysis laid the foundation for future work. Hertz made the following assumptions:

- Strains are small and within elastic limit
- Each solid can be considered an elastic half-space
- The surfaces are continuous and non-conforming
- The surfaces are frictionless

The swedish engineer Johan August Brinell proposed in 1900 a procedure to determine the hardness of materials today popularly referred to as the Brinell Test. He used a carbide ball indenter that is pushed in to the metal of interest for 10-15 seconds, leaving a mark that is later measured optically used to calculate the Brinell hardness, BNH as seen on figure 2.7. The Brinell test is usually used non-invasively on large metalparts with large grains, and its main drawback is the long test time and the difficulties to asses precise measurements of the print.

The Brinell hardness is dependent on both the load and indenter size, but it was desired that hardness should be a material property. Therefore, Meyer(b. 1875) suggested in 1908 that the hardness should be defines as

$$H = \frac{4P}{\pi d^2} \tag{2.1}$$

Meyers method also required optical post-measurements of the indentation diameter. During 1930 to 1950 Tabor [11] further developed these methods by

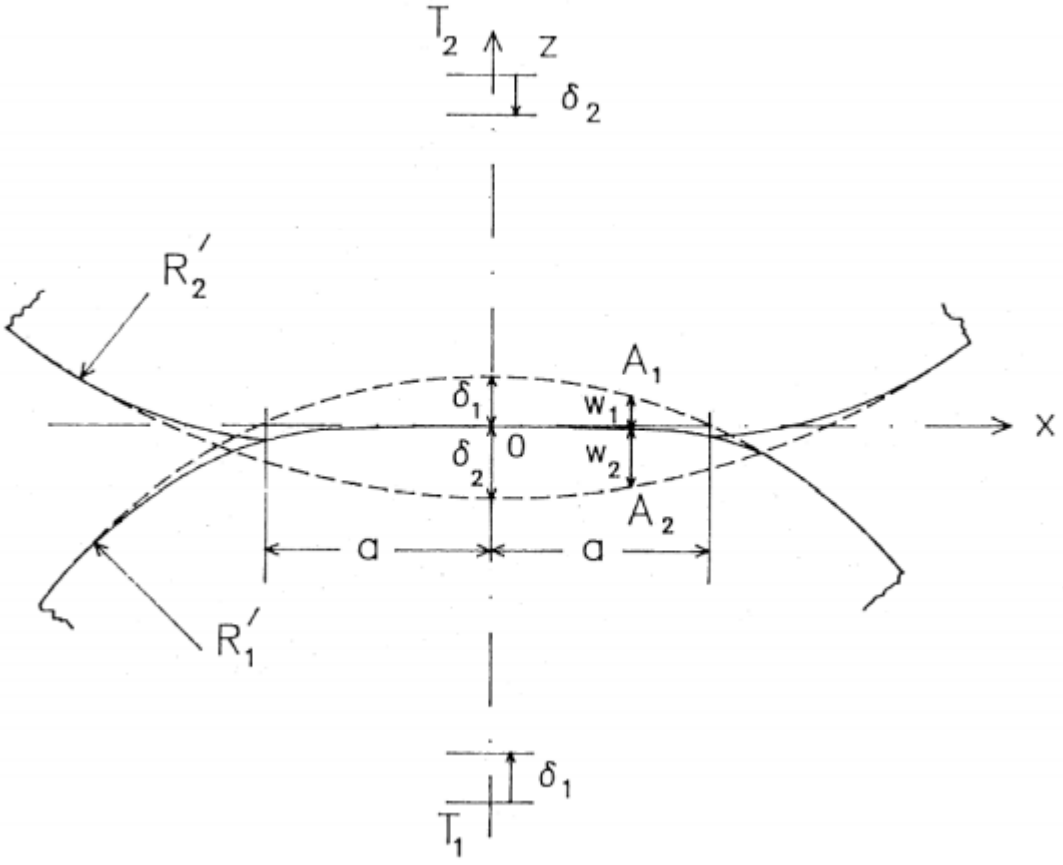

FIGURE 2.6: The study of two spheres as Hertz modeled it [9]

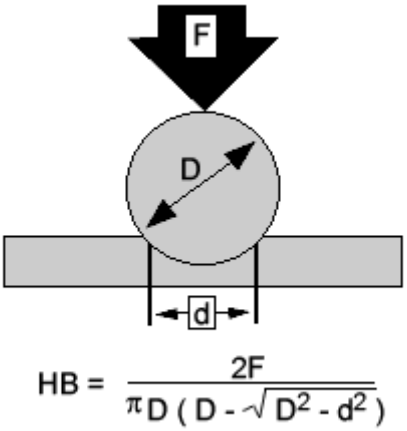

FIGURE 2.7: Illustration of the Brinell hardness test with the Brinell hardness, HB [10]

extensive testing and found that the effective strain of the indentation ϵ_i imposed by a spherical tip could be approximated by

$$\epsilon_i \approx 0.02\frac{d}{D} \tag{2.2}$$

This lead to the creation of indentation stress strain curves. By applying different loads to spherical tips and measuring the impression diameters one found that the hardness of a material which work hardens increased with increasing indentation area for spherical tips.

The Vickers test, developed in 1921 by Robert L. Smith and George E. Sandland, changed the ball from the Brinell test with a diamond that had four faces with angle 136^o [12]. They then defined hardness as

$$DPH = \frac{2Psin(136/2)}{d^2} \tag{2.3}$$

With the Vickers test, there is a scale between soft and hard materials and applicable to loads down to 50-100g. Again, the indent has to be measured optically, which is time consuming. The tip was later exchanged with the three-sided Berkovich tip, that will be described later on. The main driving force towards this change is that fabricating a diamond tip with small root raddi is less challenging for the Berkovich tip. [12]

As mentioned, both Brinell and Meyer's methods required the analyst to measure the imprinted diameter through a microscope. This is very time consuming and Stanley P. Rockwell invented the Rockwell hardness test. He was a metallurgist for a large ball bearing company and he wanted a fast non-destructive way to determine if the heat treatment process they were doing on the bearing races was successful. The only hardness tests he had available at time were Vickers and Brinell. The Vickers test was too time consuming and Brinell indents were too big for his parts [9].

The standardized Rockwell method is to use a conical diamond tip and preloading the sample to a load of 10kg to take care of the effects of surface roughness. Afterwards, a larger load is applied, and the penetration of the tip before and after this larger load is measured. This method of depth sensing lead to the development of instrumented indentation. Later, methods of instrumented indentation, where both the load and depth during indentation are measured, commonly called nanoindentation. Doerner and Nix [13]developed a method of interpreting the data from instrumented indentation where the maximum load, maximum penetration depth and final penetration depth are used to describe the indentation process. Figures 2.8 and 2.9 illustrate their ideas.

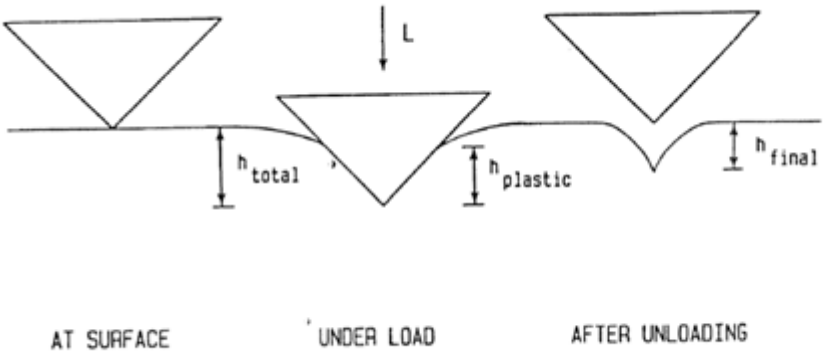

FIG. 3. Schematic representation of the indenting process illustrating the decrease in indentation depth upon unloading.

FIGURE 2.8: Doerner and Nix' illustration of the indentation with shown retracting displacement [13]

Oliver and Pharr [14] [15]further developed Doerner and Nix' methods to what is now the most commonly used procedure to calculate the hardness and elastic modulus from the load -unloading curve, known as the compliance method. Below, their method will be presented.

2.2.2 Hardware

A common indenter is the Berkovich tip, a pyramid shaped diamond tip with three sides (figure 2.11).

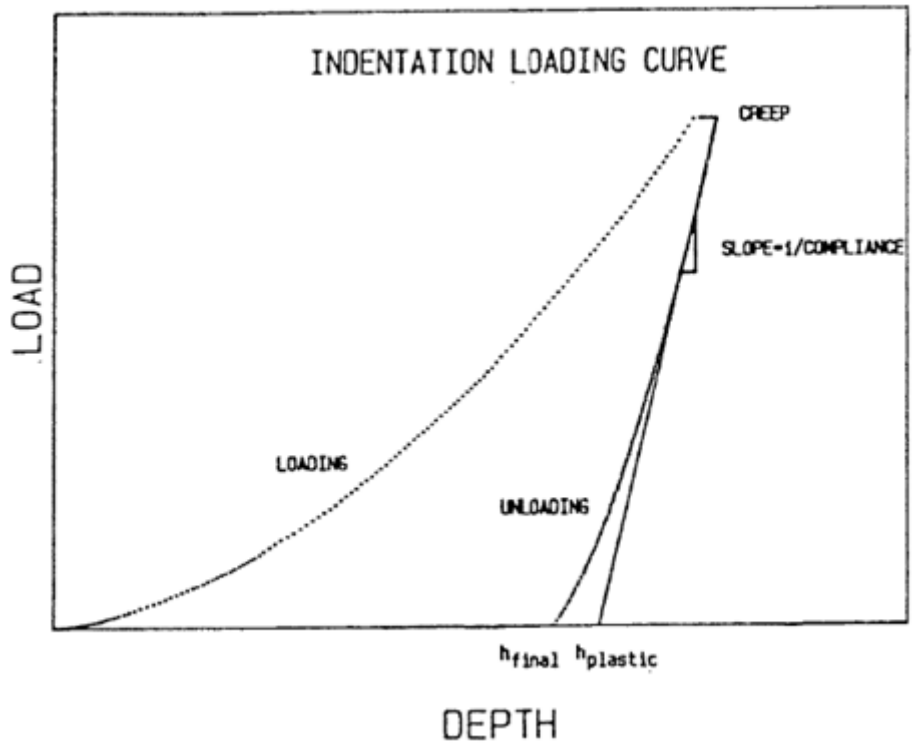

FIGURE 2.9: Doerner and Nix' illustration of a linear unloading part from [13]

Hardness is the equivalent of the average pressure under the indenter, calculated as the applied load divided by the projected area of contact between the indenter and the sample. In a conventional microhardness test, the area of contact is determined by imaging of the indentation after the load is removed and measuring the diagonal lengths. At least for metals, there is little change in the diameter of the indentation on unloading[5] so that the conventional hardness test is essentially a test of hardness under load, although it is subject to some error due to the varying elastic contraction of the diagonal.

FIGURE 2.10: Definition of hardness. From Doerner and Nix [13]

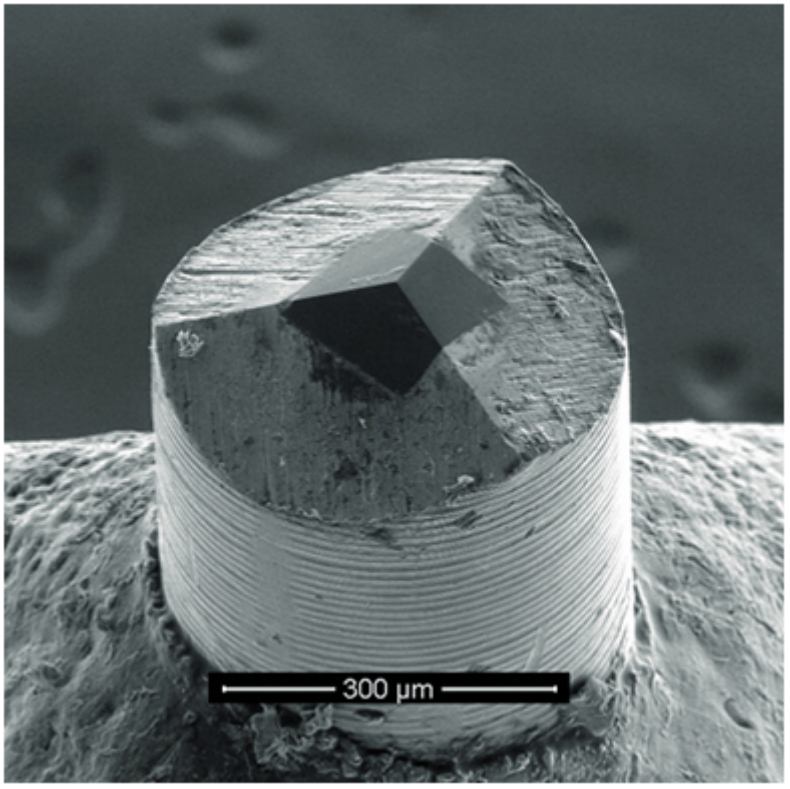

FIGURE 2.11: A Berkovich nanoindenter [16]

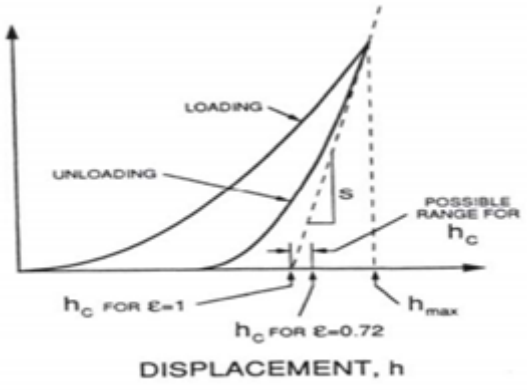

FIGURE 2.12: Different displacement positions [14]

The indentertip is connected to a transducer (figure 2.13) that through a voltage difference in the upper and lower plate moves the middle plate in which the tip is connected.

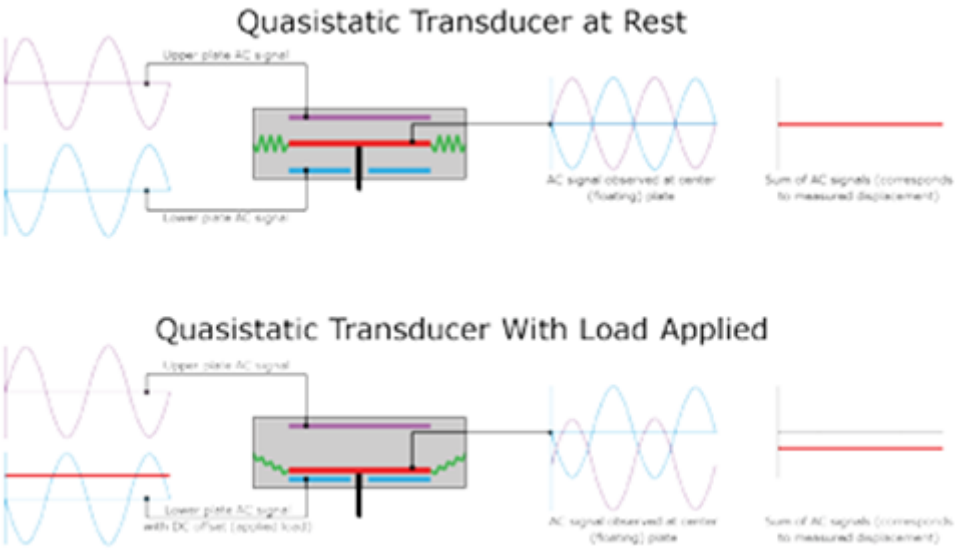

FIGURE 2.13: Illustration of the transducer that when applied, is loading the indenter. Notice the green spring, that needs to be calibrated with fused quartz [17]

The transducer is connected, together with a microscope, to a stable granite frame, and is only able to move in the z-direction. Instead, a magnetic plate that can move in the x-y plane is used as a surface. A typical setup is shown in figure 2.14.

The machine(figure 2.14) is operated through a software that gives us the ability to design both load and displacement curves which is handy on basis of which type of material we are operating on. It also gives us the possibility to automate the testing and calculates the average material properties. This can be very timesaving.

3D mapping of the surface is also available with high resolution. It is obtained by letting the indentertip trace the surface with a constant contact force, about $2\mu N$, and plotting the elevations. The results might look like in figure 2.15.

When the sample is subjected to indentation, the load-displacement curve will typically look like figure 2.16. The curve is actually thought upon as the fingerprint of the material [20]. Figure 2.16 shows two indentations of fused quartz, a very

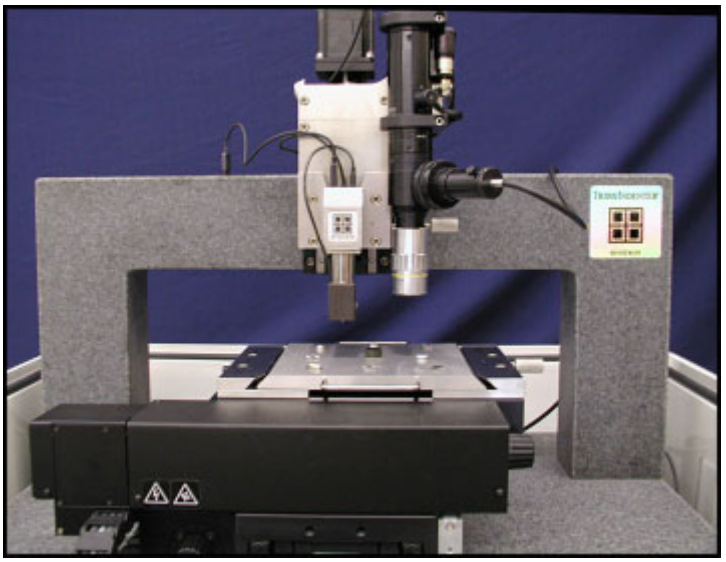

FIGURE 2.14: A Hysitron Triboindenter without protecting cover [18]

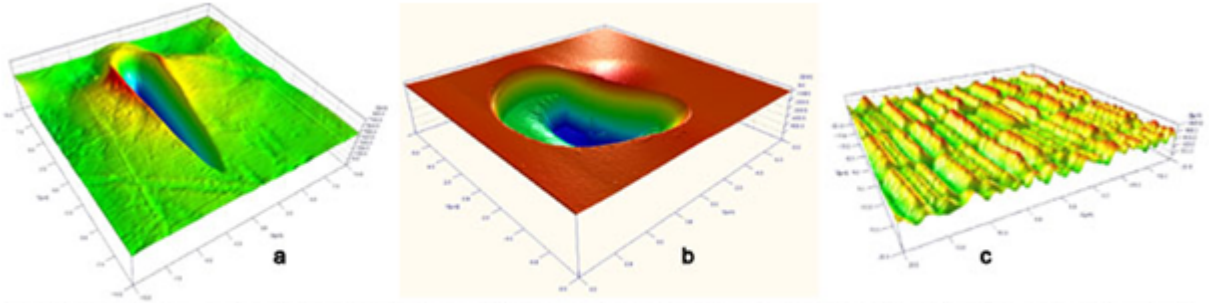

Images collected using the Hysitron AFM Imaging **a)** ramping force scratch on CNT matrix, **b)** indentation on dual-layer low-k material, and **c)** MFM image of disk drive material.

FIGURE 2.15: 3D mapping of sample surface [19]

brittle and rate in-dependent material that is often used to calibrate the transducer spring due to its elastic isotropy and has a relative low modulus-to-hardness ratio. This is seen by how parallel the two curves are. There has been done an extensive work on analyzing different materials that is often used to interpret loading-unloading curves [14].

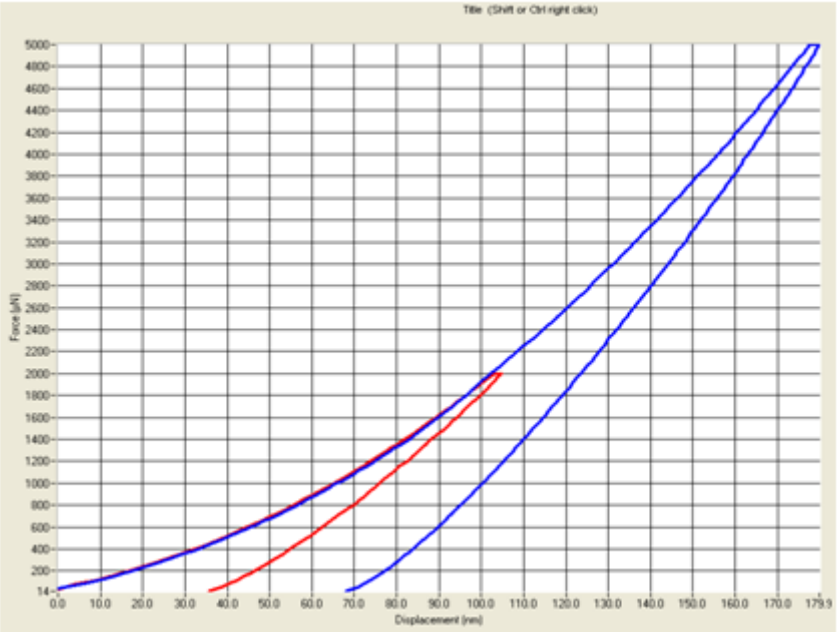

FIGURE 2.16: Displacement curves on the different tests on the fused quartz sample. (Printscreen from test run with the Hysitron Triboindenter, october 2012, NTNU.

2.2.3 Three different methods of analyzing nanoindentation data

Nanoindentation has only recently (2000-), with much credit to the work of Michelle Oyen and others, begun to include the time-dependant behavior of bone. Before, and still today, creep of materials is taken care of by adding a time delay between loading and unloading. Donna Ebenstein [21] on basis on the work of Oliver and Pharr [14] [15], has created a guide to how to do nanoindentation on biomaterial that often shows visco-elastic behaviour and therefore observable creep. Oliver and Pharr's methods are based on the assumptions that the sample materials are isotropic, elastic with negligible adhesion. Therefore, it is very important to use loading curves with a segment with constant load between the loading and unloading so that the creep rate dissipates prior to the unloading. However, more and more studies [22] [23] [24] incorporate methods of extracting visco-elastic(VE) and visco-elastic plastic(VEP) [25] material properties. Therefore, in addition to the popular method of Oliver and Pharr, the VE and VEP methods are included.

Unfortunately, not all original works are available for free, and therefore, the latter two methods are retrieved from [26].

2.2.3.1 Three different methods of analyzing nanoindentation data

According to the procedure as suggested by Oliver and Pharr [14], to calculate the hardness of material, one must use the power-function of the unloading curve. The curve should fit the power-function on the form:

$$Loading : P = \alpha h^m \tag{2.4}$$

$$Unloading : P = \alpha(h - h_f)^m \tag{2.5}$$

Where $\alpha and m are material parameters. M should have a value between 1.2 and and 1.8. h is the displac$ is the final displacement after elastic unloading, as seen on figure 2.9.

During nanoindentation, one standard assumption is that both elastic and plastic deformation occur during loading, beginning at the lower measurable loads, and that the unloading is only described by the elastic response of the system. If this is the case, then the unloading of the system can be described by

$$\frac{dP}{dh} = \beta 2 \frac{2}{\sqrt{\pi}} E^* \sqrt{A} \tag{2.6}$$

A is the projected contact area of the solid, and β is a constant that attemts to account for the differences between the axisymmetric contact models and the experimental variations in using pyramidal geometries as well as possible variations due to plastic deformation. The current accepted recommendation is that using β = 1,034 or 1,05. [14].

By arranging equation 2.6 to

$$A = \frac{\pi}{4}\left(\frac{S}{\beta E^*}\right)^2 \tag{2.7}$$

and assuming that the elastic modulus is independent of indentation depth, A has been determined empirically as

$$A(h_c) = 24,5h_c^2 + C_1h_c + C_2h_c^{1/2} + C_3h_c^{1/4} + C_4h_c^{1/8}... + C_8h_c^{1/128} \tag{2.8}$$

in this case C_1 is often chosen to fit the ideal tip shape(24,5 for a Berkovich tip). Subsequent constants are empirically selected to provide a best fit to the elastic modulus from the measured data. In the calibration process, fused quartz is a popular material to use because of its predictable and well known material properties.

The Hysitron Triboindenter includes a software that calculates every parameter for the user. One can also extract the data and to post-analysis in Microsoft Excel or Matlab for instance.

Hardness is defined by:

$$Hardness = \frac{P_{max}}{A(h_c)} \tag{2.9}$$

$A(h_c)$ is the area of the penetration at displacement h_c, given by 2.8 for a Berkovich tip.

The tangent to the unloading curve at P_{max} is given by,

$$S = \alpha m(h - h_f)^{(m-1)} \tag{2.10}$$

When the sample is unloaded, figure 2.17(b) shows elastic behavior, and a final displacement known as hf. With h_c , and subsequently A(h_c) too, we can calculate the hardness with eq. 2.9.

Finally, the reduced elastic modulus is calculated with:

$$Er = E* = \sqrt{\frac{\pi}{A(h_c}}\frac{S}{2} \tag{2.11}$$

$S = dP/dh$ is the tangent to the unloading curve, as figure 2.12 shows, and Er is the combined elastic modulus of both the sample and the indenter tip

$$\frac{1}{E_r} = \frac{1-\nu^2}{E} - \frac{1-\nu_i^2}{E_i} \tag{2.12}$$

E_i and v_i are the elastic modulus and Poisson's ratio of the indenter tip. For a dimond tip, $E_i = 1141$GPa and $\nu_i = 0{,}07$.

In 2004, Oliver and Pharr [15] reviewed their approach and discussed how their method should also be applicable with other axisymmetric indenter tips as the sphere. They also assume , for modeling purposes, that the deformation during loading is both elastic and plastic. During unloading, it is assumed that only elastic displacements are recovered. Bone is time-dependent on unloading and therefore visco-elastic. A way to circumvent this is by introducing a creep hold at peak load. Figure 2.17 shows a typical load-time curve with corresponding load-displacement curve.

2.2.3.2 The method of viscoelastic Analysis (VE)

It is assumed that with a spherical indenter, negligible plastic strains occur provided that the indentation strain is less than the yield strain. Oyen et al [26]has on this basis created a method to extract visco-elastic properties from spherical nanoindentation. The generalized standard linear model is

$$h^{\frac{3}{2}} = \frac{3}{8\sqrt{R}}P_{max}[C_0 - \sum_{i}^{2} C_i \exp^{-\frac{t}{\tau_i}} RCF_i] \tag{2.13}$$

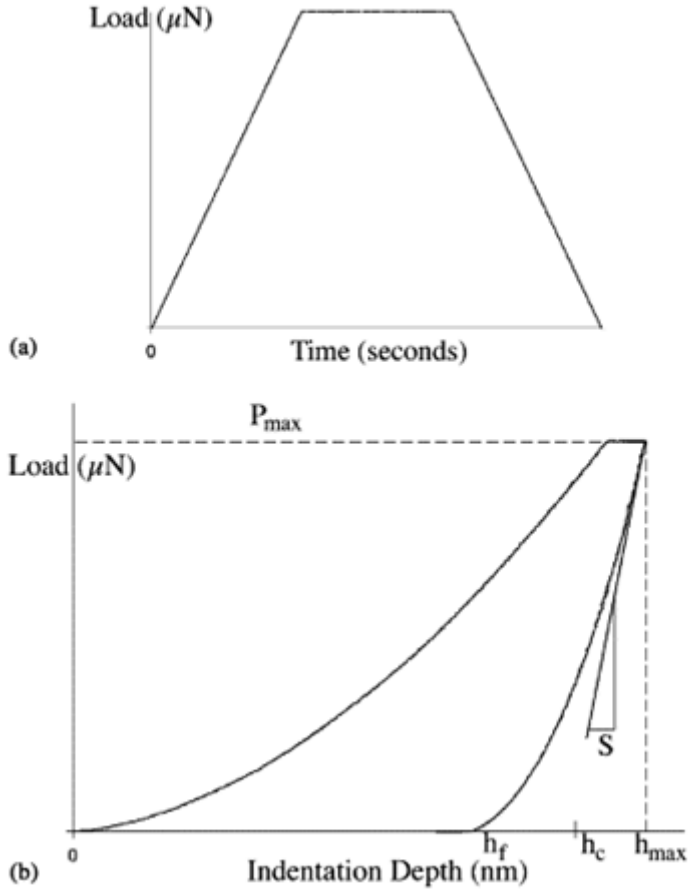

FIGURE 2.17: Load-Time (a) and Load-Displacement (b) [27]

here, R is the radius of he indenter. C_0 and C_1 are creep coefficients and are together with τ_i parameters to fit the curve.

RCF_i is a dimensionless ramp correction factor and accounts for the fact that the loading is not instantaneous. In 2007, Oyen set this to be

$$RCF_i = \frac{\tau_i}{t_r}[exp^{(\frac{t_r}{\tau_i})} - 1] \tag{2.14}$$

The instantaneous G_0 and long time G shear modulus are given by

$$G_0 = \frac{1}{2(C_0 - \sum C_i)} \tag{2.15}$$

and

$$G = \frac{1}{2C_0} \tag{2.16}$$

These are the modulus for incompressible cases ($v = 0, 5$). The ratio of these two extremes can be used to measure the degree of viscosity. If $f = \frac{G}{G_0}$ is 1, then the material is perfectly elastic. If f is 0, then the material is perfectly viscous. Bone is assumed to have $\mu \approx 0, 3$ and the calculated zero-time shear modulus $G^I(v = 0, 5)$ is translated to G^v through

$$\nu G = 2IG(1 - v) \tag{2.17}$$

The plane strain modulus is obtained from the incompressible instantaneous shear modulus

$$E^{'} = \frac{2G}{1 - v} \tag{2.18}$$

The elastic and viscous displacements are given as

$$h_{eVE} = \left(\frac{3}{16\sqrt{R}}\frac{P_{max}}{G_\infty}\right)^{\frac{3}{2}} \tag{2.19}$$

$$h_{vVE} = h_{eVE} - \left(\frac{3}{16\sqrt{R}}\frac{P_{max}}{G_0}\right)^{\frac{3}{2}} \tag{2.20}$$

The Berkovich tip is most commonly used for metals and ceramics. However, for indenting soft polymers and tissues, a spherical tip is commonly used to minimize the plastic deformation and avoid damaging the sample. The viability has been demonstrated of the recently developed data analysis method where it is argued that the spherical tip allows one to obtain measures of elastic modulus and indentation yield strength prior to the damage induced by the indentation itself [28]. This allows one to follow the evolution of the mechanical response in the material, from initial elasticity to the initiation of plasticity to post-yield behavior at

finite plastic strains. In addition to the tip geometry, the dimensions of the tip may also be important if the goal is to measure the tissue or an individual cell. As a final note, time dependent mechanical properties of bone measured at the macroscopic level have been compared with those measured by nanoindentation [23]. The results support the notion that the viscoelastic behavior of bone at the macroscopic scale is primarily due to microstructural features, interfaces, or fluid flow, rather than viscous behavior of the bone tissue. The study also demonstrates that nanoindentation provides unique data regarding the viscoelasticity of bone, but it cannot be taken as a substitute for the macroscopic behavior.

2.2.3.3 Viscoelastic-Plastic Analysis (VEP)

When using a Berkovich pyramid, the material is almost guaranteed to get plastically deformed. By using Oliver and Pharr's method, the errors might be very large if the viscosity of the material is not taken into account [29]. Therefore the following method has been suggested [29] [24]. Their method combines viscous, elastic and plastic quadratic elements in series. Figure 2.18 shows the setup.

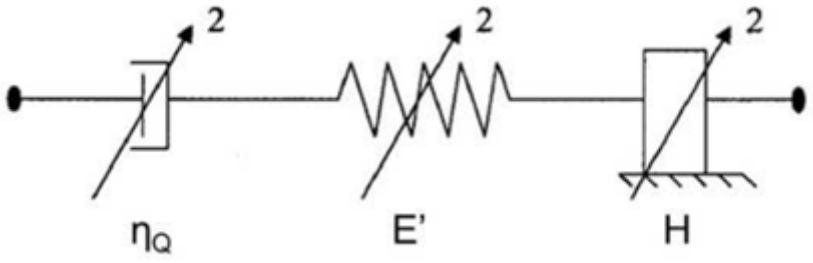

FIGURE 2.18: Illustration of the visco-elastic plastic model taken from [26]

Three time displacements equations are used to describe the loading part, the holding period and the unloading part.

$$h^{LOAD}(t) = (kt)^{\frac{1}{2}} \left(\frac{2t}{3(\alpha_3 \eta_q)^{\frac{1}{2}}} + \frac{1}{(\alpha_2 E')^{\frac{1}{2}}} + \frac{1}{(H\alpha_1)^{\frac{1}{2}}} \right) \qquad t < t_r \qquad (2.21)$$

$$h^{CREEP}(t) = \left(\frac{kt_r}{\alpha_3\eta_q}\right)(t - t_r) - h^{LOAD}(t_r) \qquad t_r < t < t_r + t_c \tag{2.22}$$

$$h^{UNLOAD}(t) = (kt)^{\frac{1}{2}}\left(\frac{t^{\frac{3}{2}} - (2t_r + t_c - t)^{\frac{3}{2}}}{\frac{3}{2}(\alpha_3\eta_q)^{\frac{1}{2}}} + \frac{(2t_r + t_c - t)^{\frac{1}{2}} - t_r^{\frac{1}{2}}}{(\alpha_2 E')^{\frac{1}{2}}}\right) + \tag{2.23}$$

$$h^{CREEP}(t_r + t_c) \qquad t > t_c + t_r \tag{2.24}$$

For a dimensionless perfect Berkovich tip (figure 2.11), $\alpha_1 = 24.5$, $\alpha_2 = \alpha_3 = 4.4$

t_r and t_c are the rising time and holding time respectively. k is the loading rate, $P_{max}t_r$. η_q is the indentation viscosity and E' is the plane strain modulus. The contact hardness is calculated for comparison with the Oliver-Pharr hardness:

$$H_c = \frac{P_{max}}{\alpha_1(h_v + h_e + h_p)^2} = \frac{1}{\alpha_1\left(\frac{2t_r}{3(\alpha_3\eta_q)}^{-\frac{1}{2}} + (\alpha_2 E')^{-\frac{1}{2}} + (\alpha_1 H)^{-\frac{1}{2}}\right)^2} \qquad t_r < t < t_r + t_c \tag{2.25}$$

Non-linear least-square curve-fit should be used and MATLAB is encouraged to use with a three step process

- η_{qis} found by fitting the holding period
- E' is obtained from the unloading curve
- keeping these parameters constant, the loading curve is then used to compute H. The viscous time constant is defined as

$$\tau_q = (\frac{\eta_q}{E'})^{\frac{1}{2}} \tag{2.26}$$

and represents the time scale of the material associated with the viscous-elastic response to indentation. For Berkovich indentations, the VEP model is divided into elastic, plastic and viscous deformation.

$$h_{max} = h_{eVEP} + h_{vVEP} + h_{pVEP} \tag{2.27}$$

where

$$h_{eVEP} = \sqrt{\frac{P_{max}}{\alpha_2 E'}} \tag{2.28}$$

$$h_{pVEP} = \sqrt{\frac{P_{max}}{\alpha_1 H}} \tag{2.29}$$

$$h_{vVE} = \sqrt{\frac{P_{max}}{\alpha_3 \eta_q}} \left(\frac{2}{3t_r + t_c}\right) \tag{2.30}$$

2.2.4 Anisotropic behaviour

As a tool to examine the local mechanical properties on the smallest levels in the bone hierarchy, nanoindentation has proved to be of great assistance, providing a very high resolution that continues to expand as the technological advances are made. Rho et al. [30] examined the elastic properties of single osteons, interstitial lamellae, and individual trabeculae of bone tissue at the microstructurural level in the longitudinal and transverse directions in addition to anisotropic behaviour of human bones. Table 2.1 shows their results.

TABLE 2.1: Mean elastic moduli and hardness for the microstructural components of cortical bone as measured by Rho et al [30]

Bone Type	Direction to Be Tested		No. of Subjects	No. of indentations	No. of Microstructural Components	Elastic modulus, GPa (SD)	Hardness GPa (SD)
Cortical bone	Longitudinal	Osteons	2	58	15	22.4(1.2)	0.617(0.039)
		Interstitial lamellae	2	58	14	25.7(1.0)	0.736(0.044)

They conclude that further testing is needed as there are uncertainties in the measurements of bone tissue by nanoindentation, including influences of elastic anisotropy. Anisotropy has proved to be difficult to measure and calculate, but efforts and progresses have been been made.

Anna Faingold et al. [31] examined the variations of Young's modulus of individual lamellae around a single osteon in three orthogonal planes in order to establish a correlation between the mechanical properties and the microstructure of the osteonal lamellae. They discovered that the modulus of the lamellae closest to the canal had the highest modulus when indentation was performed perpendicular to the osteon axis. The modulus was actually similar for all lamellae except the first. No real difference was observed in planes parallel to the osteonal axis which they suggest is due to anisotropy rather than hyperminerelization. The same tendency has later been experienced [32] in the plane perpendicular to the osteon axis, but there was also experienced different stiffness of the remnants of old osteons (22-24 GPa) compared to primary bone tissue (24-26 GPa) which they believed might serve the purpose of crack arrest. This shows that the clear picture of the anisotropic properties is not quite clear. Z. Fan et al [33] knew the bone was anisotropic and wanted to investigate the effects of elastic anisotropy on nanoindentation measurements in human tibial cortical bone and showed that the effects of anisotropy on nanoindentation measurements can be quantitatively evaluated. They developed their own mathematical model in order to describe the anisotropy of cortical bone more precisely and to consider the effects of all of the elastic constants. However, they concluded that more precise model was needed in order to establish a more general model.

In 2011, Andreas G. Reising et al [34] did an extensive work to map the orthotropic elastic properties on human cortical bone. To make the samples respond as natural as possible, minimal preparation work, except milling, was done. With 42 osteons, almost 7000 indents were made, and a table with the average values was made (Table ??).

How these results will be received will be very interesting to see.

Fabric elasticity		Engineering constants		Orientation, anisotropy	
$\overline{m_1}$	$0.748(fixed)$	$\overline{E_1}$	$10.3 \pm 0.79GPa$	$\overline{\lvert\theta\rvert}$	$10.3° \pm 0.8°$
$\overline{m_2}$	0.98 ± 0.06	$\overline{E_2}$	$16.6 \pm 1.9GPA$	$\overline{E_3}/\overline{E_2}$	1.75 ± 0.36
$\overline{m_3}$	1.28 ± 0.06	$\overline{E_3}$	$30.2 \pm 4.1GPa$		
$\overline{\mu_0}$	$6.9 \pm 0.5GPa$	$\overline{G_{23}}$	$8.6 \pm 0.6GPa$		
$\overline{\nu_0}$	$0.34(fixed)$	$\overline{G_{13}}$	$6.6 \pm 0.7GPa$		
$\overline{\epsilon_0}$	$18.46 \pm 1.4GPa$	$\overline{G_{12}}$	$5.0 \pm 0.4GPa$		
		$\overline{\nu_{23}}$	0.26 ± 0.03		
		$\overline{\nu_{13}}$	0.2 ± 0.01		
		$\overline{\nu_{12}}$	0.26 ± 0.02		

TABLE 2.2: Mean fabric elasticity parameters, engineering constants, absolute helix angle 10.3° and ratio of anisotropy $\overline{E_3}/\overline{E_2}$of the average lamella assembly material in the human femur midshaft. Borrowed from [34]

2.2.5 Viscosity and different indetation methods

Regarding viscosity of bones, and the analyzing methods that are available , there has recently been a study where the different methods were applied to mouse bone samples, in order to compare results and check for validity [26]. The models were based on the work of Oyen with partners the last seven years on the topic of creating viscoelastic(VE) and viscoelastic-plastic (VEP) models of indentation on bone samples. Differences of almost one order of magnitude were obtained through these methods as well as changing the tips, storage and expoxy the bones were embedded in. The table below, which is taken from their results show a wide spread of results through different methods on the same bone. This shows how much methods impact the results, even when the same sample materials are used.

They conclude that this makes it complicated to compare values from different studies and care must be taken when choosing the experimental and analytical options. A question that should be asked is how the bone mineral content, or the ratio between proteins and minerals in the ECM influence the mechanical properties. A study [35] demonstrated that the local Young's modulus and strain were heterogeneous at the scale of an osteon. The local Young's modulus and bone-mineral content were reasonably correlated. It was concluded that local strains cannot be described simply in terms of the bone mineral content, as the Haversian canal and osteonal microstructure have a major influence on these properties.

		Berkovich		Sphere (55µm)	
		VEP	OP	VE	OP
Dry pmma	E' [GPa]	36.4 ± 9.0	22.9 ± 3.7	7.2 ± 2.6	15.4 ± 3.7
	H [GPa]	2.57 ± 0.40			
	H_c [GPa]	0.93 ± 0.06	0.93 ± 0.07		0.17 ± 0.05
	$_Q$ (x 10^{15}) [Pa s^2]	2.96 ± 1.86			
	$f = G_\infty/G_0$			0.63 ± 0.04	
	τ_1, τ_2 [s]	277.2 ± 64.7		2.0 ± 0.8 19.6 ± 14.6	
Dry epoxy	E' [GPa]	33.7 ± 6.4	20.1 ± 3.9	6.6 ± 2.0	11.6 ± 1.7
	H [GPa]	1.91 ± 0.56			
	H_c [GPa]	0.75 ± 0.16	0.74 ± 0.19		0.15 ± 0.05
	$_Q$ (x 10^{15}) [Pa s^2]	2.53 ± 1.62			
	$f = G_\infty/G_0$			0.54 ± 0.13	
	τ_1, τ_2 [s]	252.0 ± 73.4		2.0 ± 0.7 18.8 ± 11.5	
Wet epoxy	E' [GPa]	27.5 ± 6.5	11.5 ± 2.0	4.1 ± 1.4	9.2 ± 2.4
	H [GPa]	0.47 ± 0.11			
	H_c [GPa]	0.26 ± 0.04	0.23 ± 0.03		0.10 ± 0.04
	$_Q$ (x 10^{15}) [Pa s^2]	0.50 ± 0.28			
	$f = G_\infty/G_0$			0.51 ± 0.08	
	τ_1, τ_2 [s]	133.3 ± 39 .0		2.0 ± 0.6 17.3 ± 9.0	

manuscript

FIGURE 2.19: Table of results from [26]

These results are shared by another study [36] that concluded that no single relationship can exist for prediction of modulus from composition and, conversely, there is no means to predict mineral concentration solely from elastic modulus values.

Finally, adhesion between the sample and the tip should be taken into account as it may create a negative load in the beginning of the loading and in the end of the unloading curve. Force curve methods widely used in AFM is suggested to apply for nanoindentation [21].

Chapter 3

Materials and methods

3.1 Introduction

This chapter addresses the procedure of nanoindentating mice femur and the analysis of the obtained data. At the end, the results are compared with other studies and discussed, and finally, improvements on future testing are suggested.

3.2 Sample

Three mice femur were chosen to be tested. These were not part of the project (section 1.1) and only meant for testing purposes. They were subjected to different conditions, such as maximum load and physiological condition, ie. dry or wet. Table 3.1 gives an overview of the different scenarios. The method number refers to the group of six indentations, as the figure 3.2 shows. From here on, the mice femur will be reffered to as "'sample"' and index.

index	Force[mN]	Condition	Number of indentations	Method(s)
1	1	Wet	6	9
2	10	Wet	12	6,8
3	10	Dry	12	6,8

TABLE 3.1: Record of the samples and their test conditions

3.3 Preparation of the sample

The samples were received from St. Olavs hospital and prepared for nanoindentation, as described below.

They were covered in fabric and left in a PBS solution until saturation. They were then stored in a freezer holding $-18°C$ until the samples were ready to be tested. At roomtemperature, they were put back in the PBS solution for 18 hours to defrost.

Depending on whether or not the sample was chosen to be wet or dry tested, it was either put back in the PBS solution (for wet condition) or air dryed(for dry condition).

Each sample was put, and kept steady, in an aluminium container filled with epoxy until it had solidified, like figure 3.1 shows. Using polishing paper, the surface was manually polished for an hour using silicon carbide paper with finer and finer coarseness until the surface was reflective. The grades used were 320, 500 and 4000. Now, the samples were ready to be tested with the nanoindenter.

3.4 Nanoindentation

Six nanoindentations were done on sample 1 and 12 indentations were done on each of the two other samples. For sample 2 and 3, six indentations were done at the medial and lateral side of the femur as shown figure 3.2. The exact placement of the indentations are considered random since the manual polishment made it

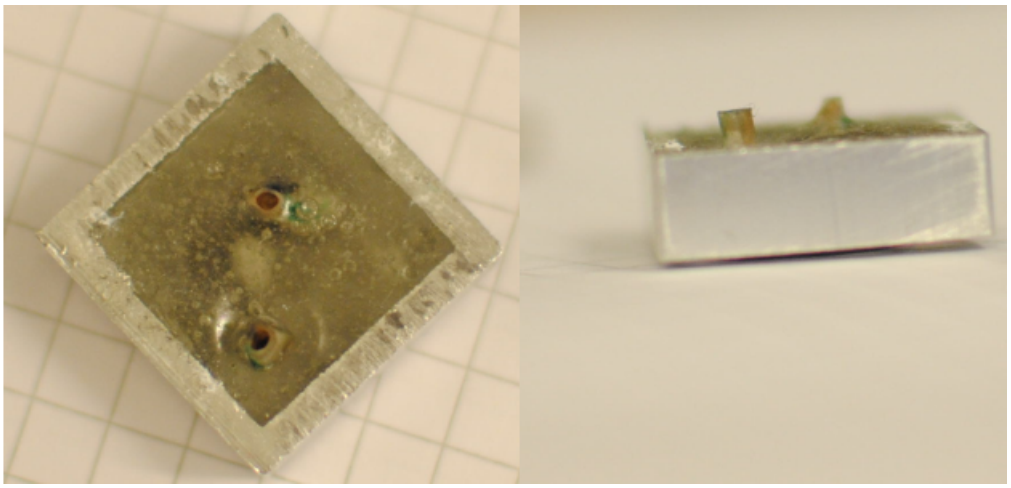

FIGURE 3.1: Bone in epoxy viewed from top and side

impossible to distinguish the bone matrix, but the goal was to collect the samples as close as possible to each other to eliminate heteregenous influence.

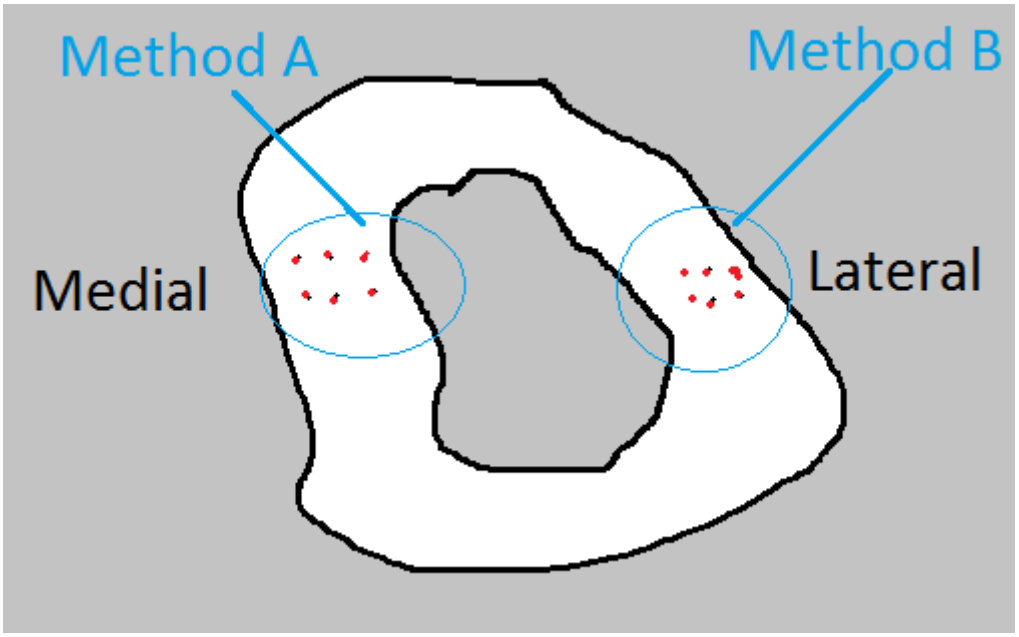

FIGURE 3.2: The placement of the indentations are shown as red dots on a cross section of a sample. Six indentations were done at at each group, positioned at the medial and lateral side of the femur. The groups are called methods and are labeled with a separate number

Since the main goal of the testing was to determening the indentation modulus, a berkovich tip was chosen. The acuteness of this indentertip counter the

viscous effects by imposing large amounts of shear(and thus driving plastic deformation) [24]. In addition, critical assumptions were made when choosing to analyze the samples as elastic plastic materials [37]:

- The constitutive behaviour of the sample is elastic with time-independent plasticity.
- The solution for the elastic deformation of an irreversibly indented surface geometry is similar to the one of a flat semi-infinite half space
- The Poisson ratio ν is known.

3.4.1 Preparation

The hysitron 4000 was automatically calibrated [14] using fused quartz, which is known to have an indentation modulus of 72GPa. Then, the load function had to be defined. We chose 30 seconds loading to the maximum load (depending on the sample), 50 seconds resting and 30 seconds unloading, as illustrated with figure 3.3. Bone is known to be viscous [24] [38] and therefore, to minimize the viscous effect on the elastic unloading curve, the holding, or resting time, is important to minimize the effects of viscoelasticity. Also, this technique will pick up, and let the machine correct for any thermal drift.

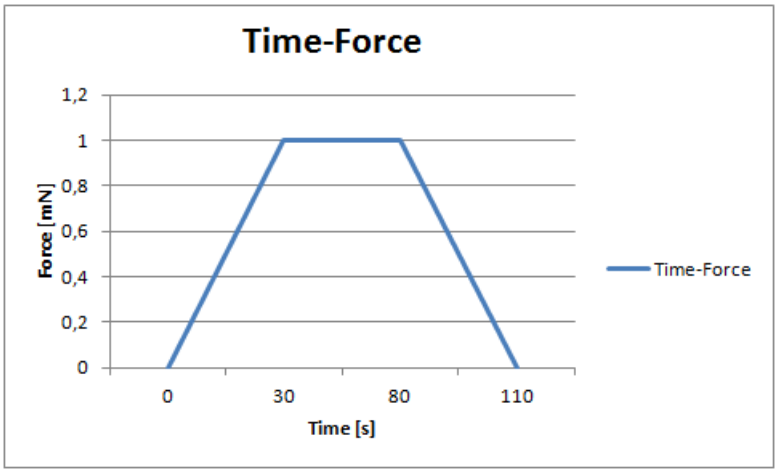

FIGURE 3.3: Illustration of the load-time curve. The load and unload times are identical, 30 seconds. To reduce visco elastic influence, there is a hold time of 50 seconds between loading and unloading. For one sample, a load if maximum 1mN is applied. For the other samples, the load is set to 10mN

Even though biological material is likely to exhibit significant viscous deformation [24] [38] , the object was to determine the global and local stiffness. Therefore, after the procedure, the Hysitron software calculated all data and asscociated material properties using the procedure of Oliver and Pharr [14]. Typically, the software uses from 20% to 95% of the unloading curve to calculate the unloading tangent, S (equation 2.10). Poisson's ratio of 0.3 was used in this study, which is consistent with other reports. The relative error by varying it from 0.2 and 0.4 ranges from 9.9% to -8.2% [39] [40].

3.5 Results

Below are the results from the testing.

TABLE 3.2: Indentation results of 1 mN wet

Indentation	Force[mN]	$h_c[nm]$	Max displacement [nm]	$E^*[GPa]$	Hardness[GPa]
9 0000	1	274.08	291.56	31.96	0.75
9 0001	1	201.02	221.92	35.55	1.23
9 0002	1	205.25	218.81	52.58	1.19
9 0003	1	122.12	153.03	35.09	2.58
9 0004	1	86.36	101.15	94.68	4.32
9 0005	1	119.54	129.96	103.22	2.67

TABLE 3.3: Table of results from sample 1

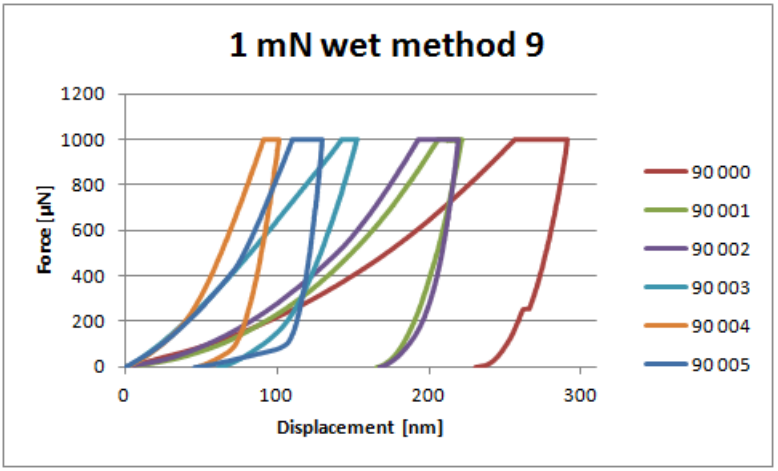

FIGURE 3.4: Collection of all load-displacement curves sample 1

TABLE 3.4: Indentation results of sample 3 method 6 and 8

Indentation	Force[mN]	$h_c[nm]$	Max displacement [nm]	$E^*[GPa]$	Hardness[GPa]
6 0000	10	522,43	613,67	34,02	2,25
6 0001	10	557,14	648,27	32,26	1,98
6 0002	10	597,84	690,83	29,42	1,71
6 0003	10	544,21	631,46	34,25	2,07
6 0004	10	536,34	622,57	35,42	2,14
6 0005	10	558,87	640,90	35,74	1,96
8 0000	10	729,28	820,31	24,42	1,13
8 0001	10	668,09	768,60	24,22	1,36
8 0002	10	521,25	599,97	40,27	2,26
8 0003	10	636,48	726,29	28,51	1,50
8 0004	10	541,00	626,29	35,16	2,10
8 0005	10	539,27	624,63	35,66	2,11

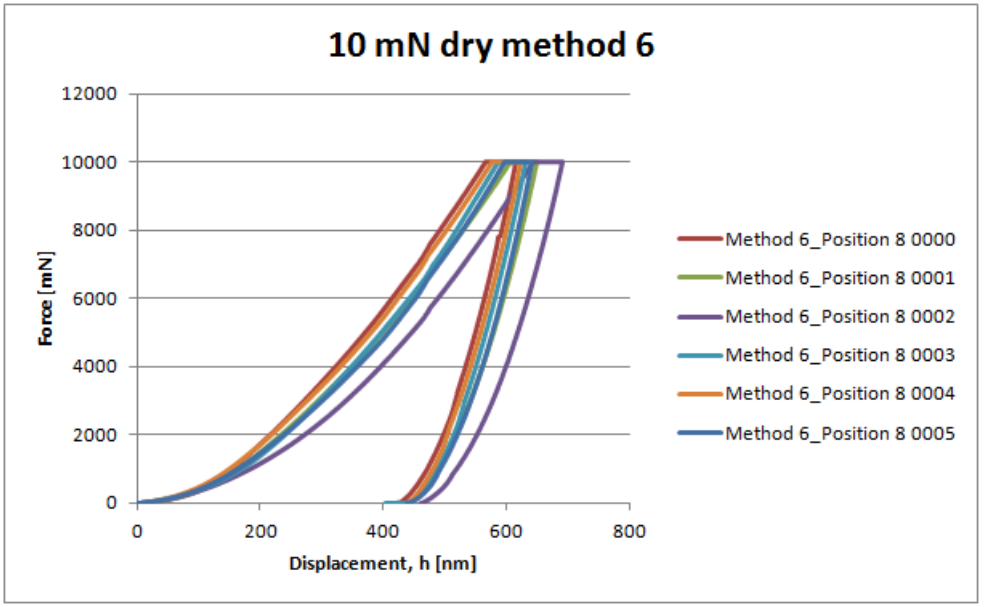

FIGURE 3.5: Load-displacement curves from sample 3 method 6

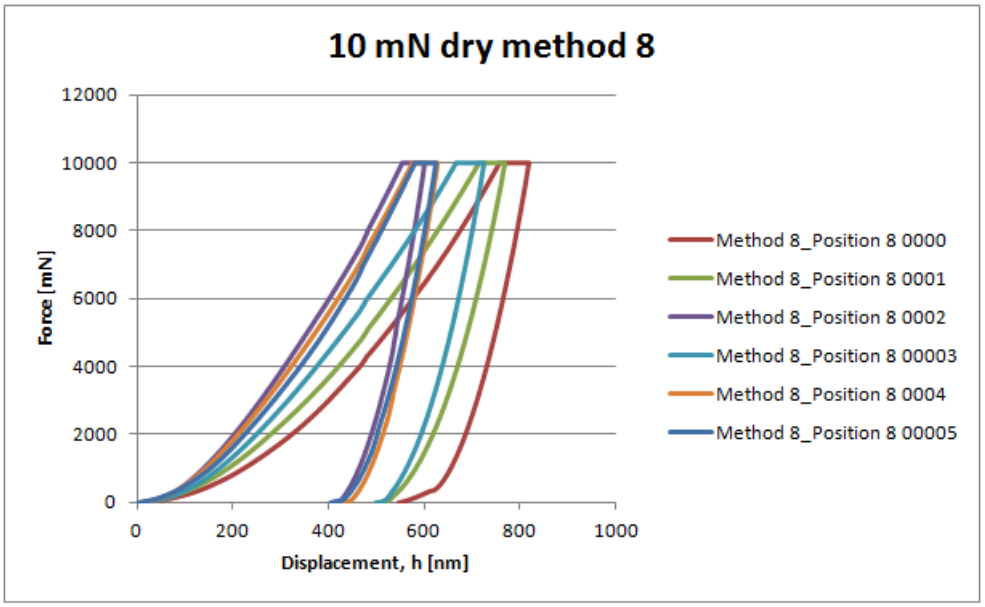

FIGURE 3.6: Load-displacement curves from sample 3 method 8

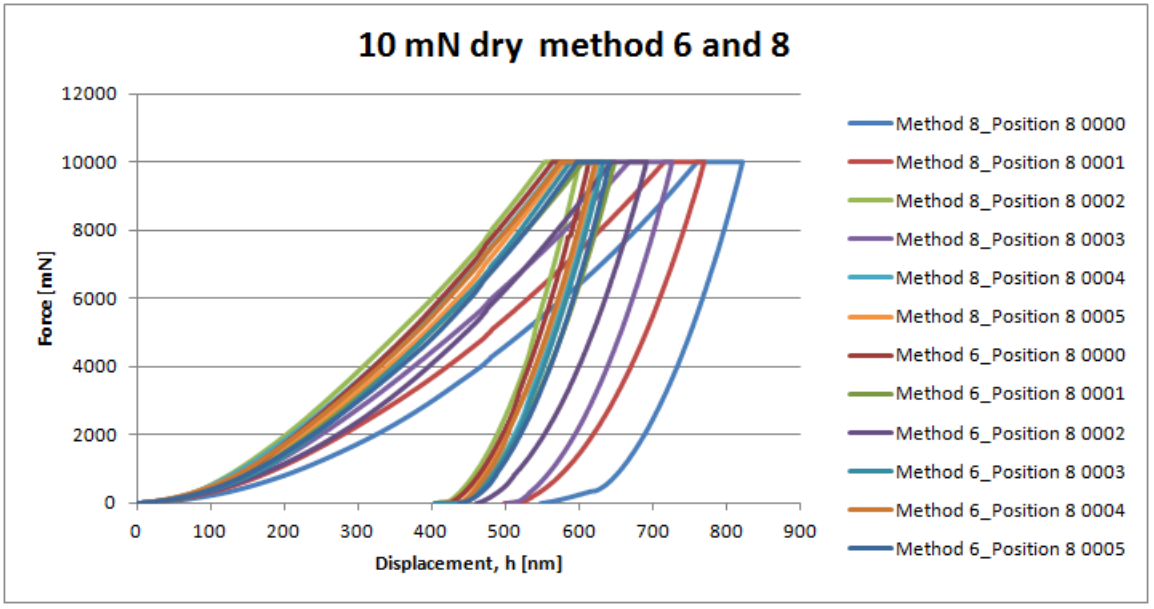

FIGURE 3.7: Load-displacement curves from sample 3 together

TABLE 3.5: Indentation results of sample 2, method 6 and 8

Indentation	Force[mN]	$h_c[nm]$	Max displacement [nm]	$E^*[GPa]$	Hardness[GPa]
8 0000	1	805,62	890,87	23,16	0,91
8 0001	1	790,48	868,21	26,39	0,95
8 0002	1	743,00	812,73	31,08	1,09
8 0003	1	906,42	992,13	20,40	0,71
8 0004	1	658,04	732,13	33,33	1,40
8 0005	1	723,61	794,62	31,37	1,15
9 0000	1	687,97	755,44	34,73	1,28
9 0001	1	622,21	693,59	36,75	1,58
9 0002	1	723,73	802,56	28,38	1,15
9 0003	1	653,19	727,89	33,38	1,42
9 0004	1	719,38	782,15	35,73	1,16
9 0005	1	631,47	704,23	35,48	1,53

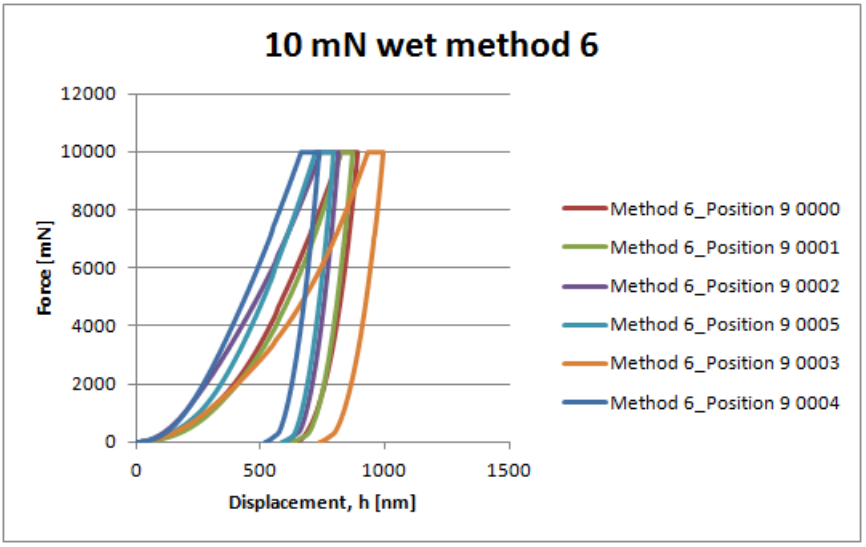

FIGURE 3.8: Load-displacement curves from sample 2, method 6

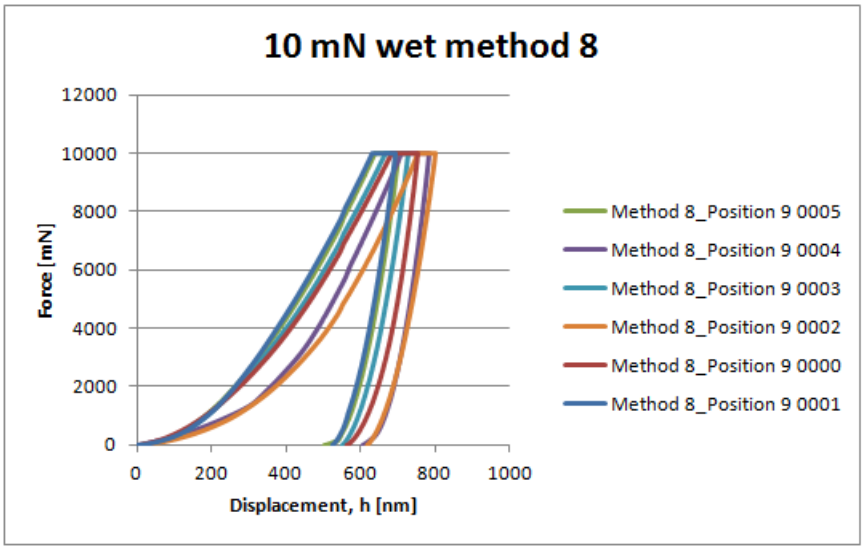

FIGURE 3.9: Load-displacement curves from sample 2, method 8

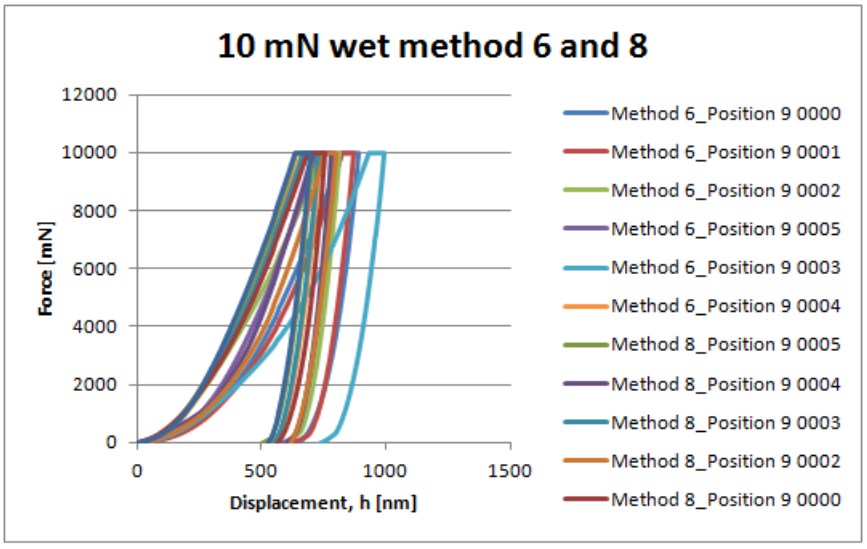

FIGURE 3.10: Load-displacement curves from sample 2, together

3.6 Statistical analysis

Computing the mean value was done using

$$\mu_x = \frac{\sum_i^n x_i}{n} \tag{3.1}$$

the standard deviation was calulated through

$$\sigma_x = \sqrt{\frac{\sum_i^n (x_i - \mu_x)^2}{n-1}} \tag{3.2}$$

and the standard error is given by

$$SE = \frac{\sigma_x}{\sqrt{n}} \tag{3.3}$$

The results are presented in the table below.

Table 3.6: Mean and Standard Deviation

Value	Test	$h_c[nm]$	Max displacement [nm]	$E^*[GPa]$	Hardness[GPa]
μ_x	1 mN wet	168,06	186,07	58,85	2,12
	10 mN wet	722,09	796,38	30,85	1,19
	10 mN dry	579,35	667,82	32,45	1,88
σ_x	1 mN wet	70,49	70,62	32,01	1,33
	10 mN wet	82,18	86,59	5,24	0,26
	10 mN dry	65,8	69,39	4,87	0,37
SE	1 mN wet	28,78	28,83	13,07	0,54
	10 mN wet	23,72	25,00	1,51	0,08
	10 mN dry	19,00	20,01	1,41	0,11

FIGURE 3.11: The results from table 3.6 graphically illustrated. The samples are here described by their conditions

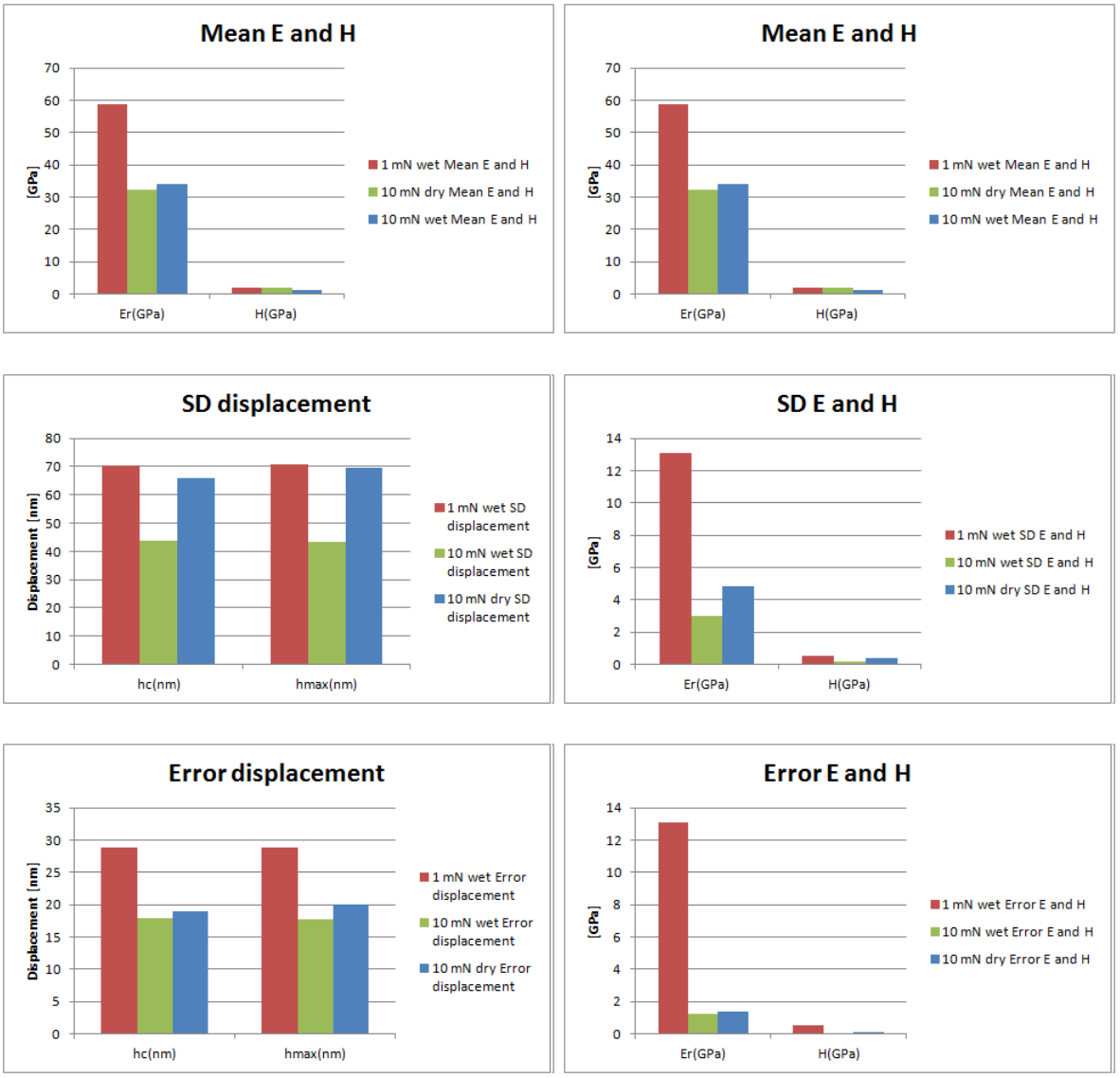

3.7 Discussion

Three bone samples have been tested with different conditions, as described with table 3.1. The results show that sample 2 and 3 are much more consistenct than sample 1. For sample 1, the elastic modulus varied between $31,96GPa$ and $103,22GPa$ with a mean of 58,85GPa and standard deviation of 32,01GPa. Compared to the other samples, this deviation is almost six times larger. However, because surface roughness changes its relative influence with increasing depth, the standard deviations of the results should also show a depth dependence [41]. Still, it is questionable that the roughness should influence the difference to such a degree.

When curve fitting the reduced elastic modulus, E*, as a function of maximum displacement, h_{max}, in Microsoft Excel, sample 1 also lacks consistency compared to the two other samples. Linear regression gives the following trendlines for each bone sample (figure 3.12 and table 3.7).

TABLE 3.7: Record of linear correlation between E^* and h_{max} as a function of displacement, h

Sample	Indentations	E*	R^2
Wet 1 mN	6	-0,3459h + 123,2	0,5823
Wet 10 mN	12	-0,0662h + 76,639	0,8886
Dry 10 mN	12	-0,057h + 76,234	0,8855

It is also easy to see the differences when comparing the samples, as seen on figure 3.11.

Table 3.7 shows that the coefficient of determination for sample 1 is much poorer than the other two ($r^2_{sample1} = 0,5823$ compared to $r^2_{sample2} = 0,8886$ and $r^2_{sample3}$ =0,8855). This might have been caused by many factors. The surface area might have been too coarse due to poor polishing. This would result in a topography that reminds of peaks and valleys. The indentations would be greatly affected by such differences in topology. The literature [39] [42] reports of poorer results when the depths measured are between 100nm and 250nm and much more consistent with depths ranging around 500 nm. This seems to agree with our results. They also

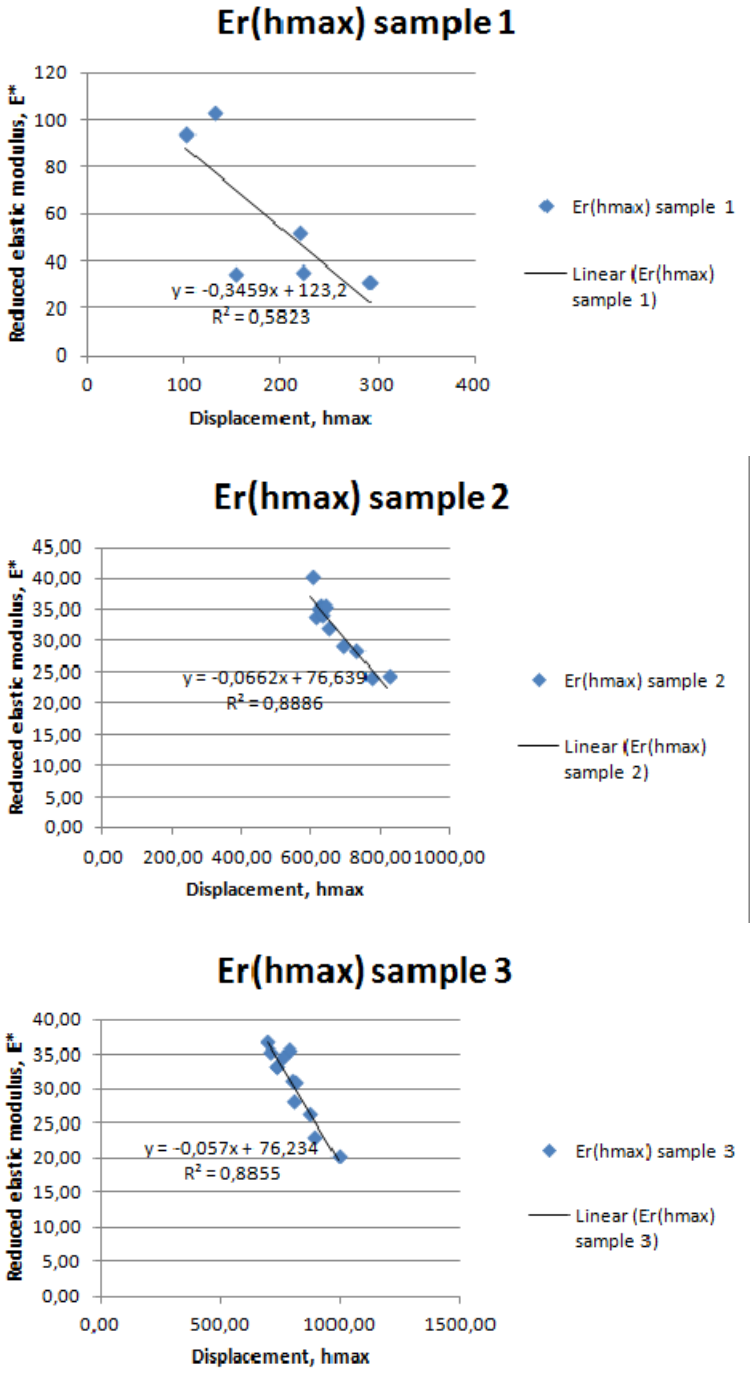

FIGURE 3.12: Correlation between maximum displacement and reduced modulus for all samples

leaves the open question of the small depth variations alternatively may represent biological variability of true mechanical significance.

Finally, it should be noted that the results also might be a product of a too small sample pool. All in all, it was determined to ignore the results from sample 1.

Regarding the two other bone samples, their results were, as already mentioned, much more consistent. With a mean reduced modulus for the wet and dry at 30,85 GPa and 32,42 GPa, and a standard deviation of 5,24 GPa and 4,87 GPa, respectively. Still, this deviation is quite high, 17% for the wet bone and 15% for the dry bone, compared to fused quartz with a standard of 2% deviation. This is probably due to local variations related to mineral, collageneous nad noncollagenous protein composition. It has been reported different indentation moduli within an osteon as the distance from the center increases [31] [42] and. Since the osteon is developed from the center and out, the innermost lamella is also the newest one, with the highest level of mineralization. L. Feng et al [43] and [41]discovered that there was a consistent difference in elastic modulus and hardness between thick and thin lamellae where the thick showed larger values than the thin. Again, this might explain some of the differences. Another factor that should be included is that of bacterial degradation when the measurement period exceeds a few hours ([37]).

It is interesting to see that E^*, h_{max} and H are all affected by the samples physialogical condition, which is supported by the literature [37]. Hoffler et al [39] reported of a indentation modulus of 17.7 ± 4.0 GPa for osteons, and 19.3 ± 4.7 GPa for interstitial bone tissue. The dry specimen returned significantly higher indenation moduli and hardness than the wet specimen, 22.6% and 56% higher values respectively. The increased hardness might be due to the dehydrated collagenous bone tissue component decreasing in the compliance of bone collagen-mineral composite Hoffler et al [39]. [42] reported of 21.1 ± 2.0 GPa and 24.4 ± 2.2 GPa for respectively wet and dry osteons. This results in an increase in modulus of approximately 15% . Compared to the results from this study (5.19% and 58.0%), the increased hardness seems appropriate. For the modulus, the results are not as

clearly in agreement with the literature. One can only speculate why the difference in elastic modulus is so small for the dry and wet specimen, but it is important to notice that it has in fact increased. Just not as much when compared to other studies.

Comparing our results with other results from nanoindenation of mice, the values are encouraging. Pathak et al. [44] reports of approximately 30 GPa and 22 GPa for the modulus of two different strains of mice. This study was done with a spherical indenter to minimize plastic influence. As mentioned in chapter 2, it was concluded that this makes it complicated to compare values from different studies and care must be taken when choosing the experimental and analytical options [26]. Middleton et al [45] reports of mean elastic moduli between 29.78 and 33.09 GPa. For human bone, the elastic modulus has been found to depend strongly on tissue type, anatomical location and individual [37]. Since our test protocol did not include a specified region of the bone that was to be indented, the results might have been affected and therefore harder to compare with other results from mice.

Figure 3.13 shows a significant correlation between reduced modulus and hardness for both samples. With r^2 found to be 0.8762 and 0.7961 for the dry and wet bonesamples, respectively, they both exceed the results found in the literature [39] [37], which is comforting.

FIGURE 3.13: Correlation between reduced moduli and hardness for both samples measured at 10 mN

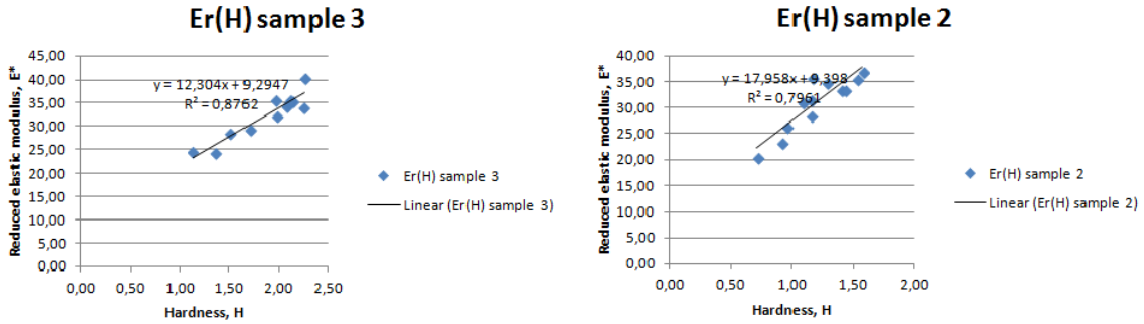

A potential limitation of the method is pile-up at the edge of the indenter when the material has too high of a ratio of effective modulus over yield stress [40] [12]

while annealed materials which have high work hardening exponents tend to sink in around the indenter. This is a result of excessive material being pushed up as the sample is indented. The issue surrounding pile up is in regard to determining the proper indented area that is used to calculated the reduced modulus [46]. Unfortunatly, for this study, it has not been possible to aquire imagery of the indentations. Therefore, this might be a factor to the inaccuracy.

Finally, as mentioned in chapter 2, using a Berkovich pyramid, the material is almost guaranteed to get plastically deformed. By using Oliver and Pharr's method, the errors might be very large if the viscosity of the material is not taken into account [29]

In conclusion, the tests have revealed some weaknesses, and showed some strengths. The goal of these tests was not to improve the understanding of the mechanical properties of femur bone as much as preparing for a protocol that will provide stable and predictable results that are highly comparable with each other. Since the mission of the overall project is to compare bone samples with another, the most important factor is to minimize the variations of measured moduli, even though it self might not prove useful compared to other results found in the literature. However, in regard to improving the accuracy of the measurements, the indentation protocol should be adjusted. Avoidance of lamellae with different thickness is encouraged. Also, keeping the displacement range to approximately 500 nm is too. Since the indentations are load-controlled, this means the load should be set and kept consistantly. This is also adviced since bone is rate dependant [39] Antibacterial methods should at least be considered when planning the tests if multiple hours are expected to spent on measurement. The section of the bone sample should also be considered and kept consistant for accuracy [43] [32].

Chapter 4

Finite element modeling of nanoindentation

4.1 Introduction

Finite element modelling has become a popular means to investigate the material properties of a subject. In this chapter, a model has been made in Abaqus in order to investigate elastic and plastic behaviour. The bone was modelled as an isotropic homogeneous elastic perfectly plastic material. Although bone is considered anisotropic and heterogenous with viscoelastic behaviour, a simple model might prove useful when comparing the elastic modulus extracted from experimental results. As the experimental test procedure was chosen such that the material would exhibit dominantly elastic plastic features, an FE model with the same properties seems fitting. The goal of this study was to determine the strengths and weaknesses of the model and see which areas, if any, would be helpful on improving the understanding of bone indentation. This is discussed in a later chapter.

4.1.1 The model

In the experimental indentations, the bone was surrounded by solidified expoxy in an aluminium box, as previously seen on figure 3.1 on page 31. Figure 4.1 illustrates a section of the sample in epoxy with an axis of symmetry. Since the indentation area is much smaller than the size of the whole bone, only a small part of the sample was modeled.

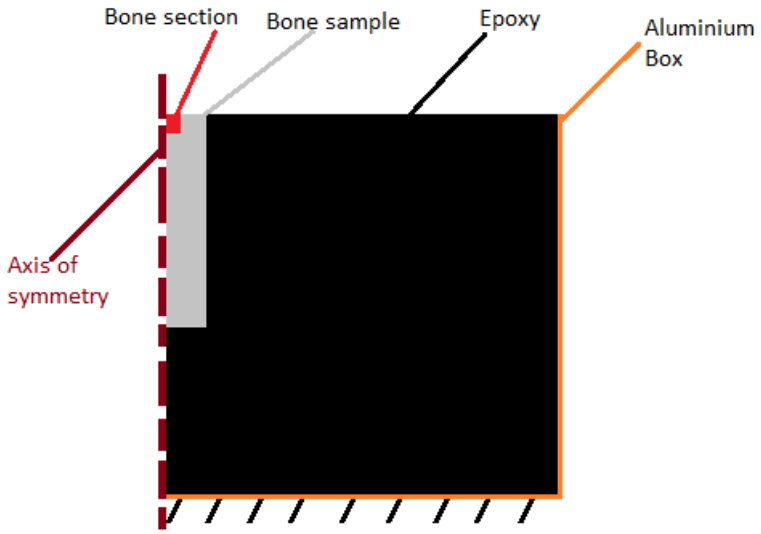

FIGURE 4.1: An illustration of the model. The bone is submerged in epoxy in an aluminium box. The bone section is the part that was modeled, and is seen at top, next to the axis of symmetry

The size of this bone section was chosen based on previous [47] work where convergence of the results was tested by varying both the dimensions and mesh of the model. It was shown that the ratio between the shortest side and the indentation depth should not be below 40 in order to be safe from far field effects from boundary conditions (figure 4.2).

Since the displacement depth was averaging at around 600 nm, an axissymetric rectangle part representing the bone was modelled with dimensions 200 μ meters in height and 200 μ meters in length. With these dimnensions, the ratio between size and depth exceeds 300 - far over 40.

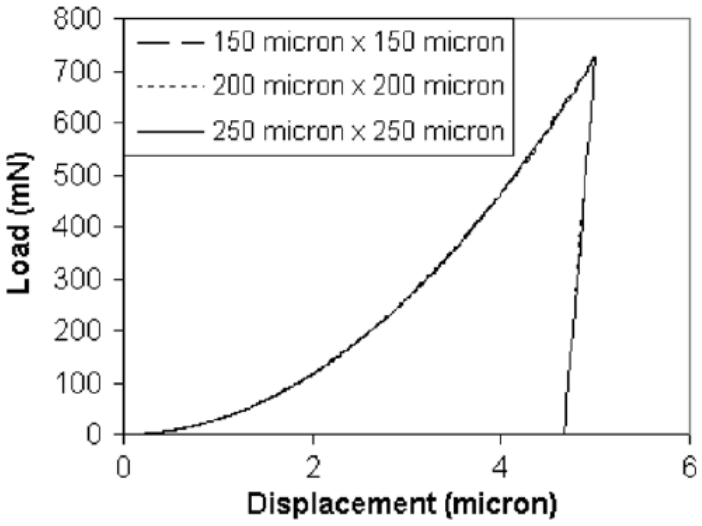

FIGURE 4.2: Studies of sensitivity to far-field effects for conical indentation from [47]

It has been shown [47] that 2D axisymmetric model with 70.3 degrees gives the same results as a 3D model with Berkovich indenter. They do however experience that insignifficant discrepancies will occur when including strain hardening. This is not an issue in this study since the model is perfect plastic. This allows us to create a much simpler 2D model that is easier to analyze. The model and procedure was inspired by the procedure of [48] that showed that by using a damage plastic model the max force was 10% reduced compared to a perfect plastic model. This damage plastic model was not applied in this study.

Figure 4.3 shows the bone section from figure 4.1 at a closer look. Based on gathered information, it was chosen to model it axissymmetric, with the bottom encastred, and the left side - facing the axis of symmetry, with only vertical displacement. The right side was left untouched because the size of the model was chosen so that the far field effects were negligible.

The model was built on the following assumtions:

- there is no strain hardening of the marials used in model
- there is a perfectly interfacial bonding between the indenter and the substrate.

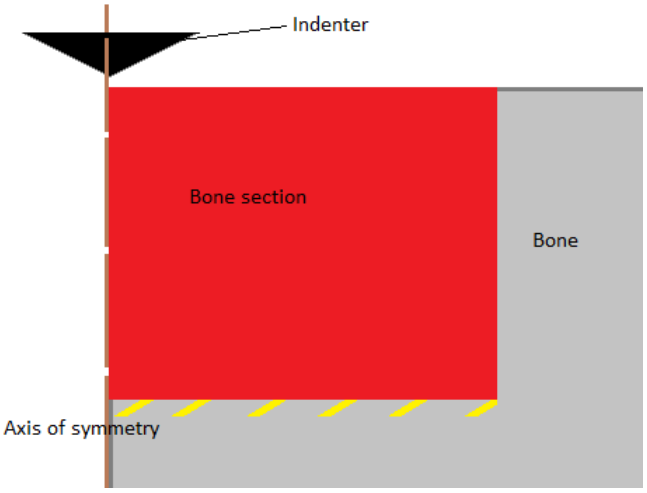

FIGURE 4.3: A closer look at the bone section that was modeled

- there is no interaction between the bone and the epoxy due to the indentation, and the epoxy is therefore not included in the model.

4.1.2 Choosing the geometry

In Abaqus, a new model was created with two parts; an axissymmetric rectangle of 200μm X 200μm to avoid far field effects and an analytical rigid indenter(figure 4.4) were created.

The indenter was modeled as an axisymmetric analytical rigid part with an angle of 70.3^o as figure 4.4 shows. A reference point was picked (as seen on the figure) at the part so that it could be used later to define the vertical displacement of the indenter.

4.1.3 Material

An isotropic perfectly plastic model was chosen. In order to get started with the testing, an elastic modulus of 30GPa was chosen. This was inpired by the results from the experimental tests. The yield strength was chosen to be 150MPa. This was just a starting point that would later be corrected when attempting to match the experimental curves with the analytical results.

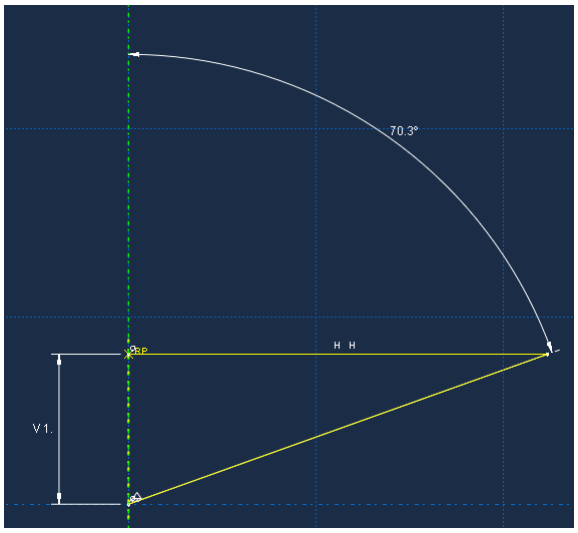

FIGURE 4.4: Geometry of indenter

A diamond identer, with a Young's modulus of 1141 GPa, is almost rigid compared to the bone, and was therefore modeled as an analytical rigid part.

4.1.4 Mesh

To get the curve as smooth as possible, a graded grid with finer grid size where material was indented, was chosen as figure 4.5 shows. To be able to make this grid, the part was partioned and then seeded manually.

The elements chosen were CAX4R - four-node, bi-linear axisymmetric quadrilateral elements. 60025 finite elements were created upon meshing. There were issues surrounding small time steps caused by too distorted elements in the contact area when the mesh was extremely fine. To circumvent this, the mesh was made coarser, but fine enough so that the results were not affected.

Figures 4.10 and 4.11 show choppy loading curves. This was the result of the mesh being too coarse. When comparing the model with the experimental results from chapter 3, a much finer mesh was chosen, and the loading curves became much smoother.

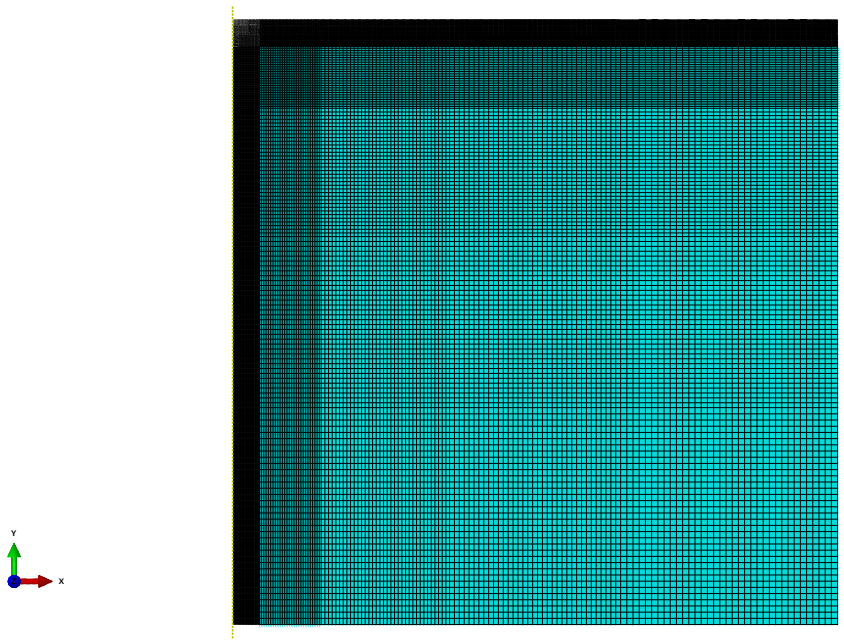

FIGURE 4.5: Mesh

4.1.5 Assembly and contact definitions

The two pieces were assembled and surfaces were chosen which makes setting boundary conditions and choosing contact surfaces easier. A rigid body constraint was applied to the indenter, and contact controls for stabilisations was created with Automatic stabilization set to 0.001.

The interaction between the indenter and the plate was assumed frictionless [40] and a surface to surface interaction. Friction has an effect on the hardness value, but not on the loading curve [47]. The indenter was chosen as the master surface, and the top surface of the plate was chosen as the slave surface. This way the plate was sure not to penetrate the indenter.

4.1.6 Boundary conditions and displacement

The bottom was encastred so that it was not able to move in any directions. The left side was set to be free in the y-direction, with neither rotational or horizontal movement. As a result of no far field effects, the right side was kept untouched.

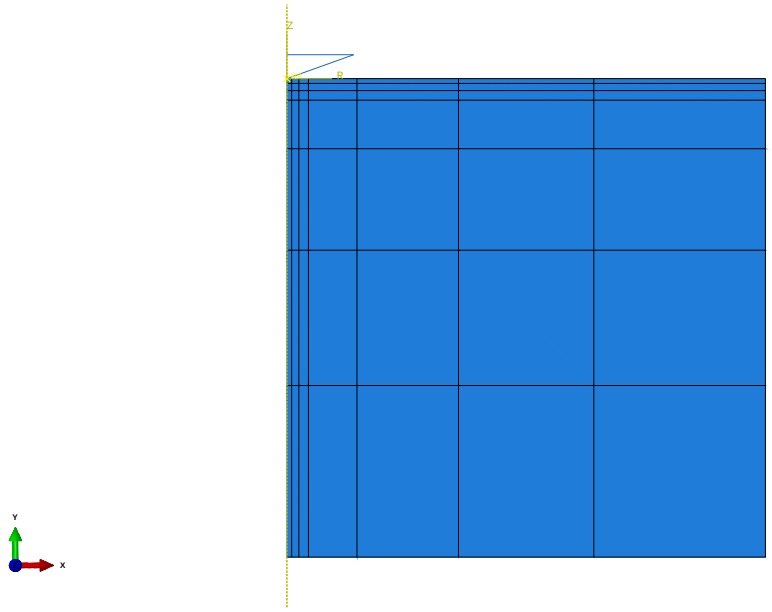

FIGURE 4.6: Assembly

The indenter was also not able to rotate, nor move horizontally. Vertical displacements corresponded to loading and unloading.

Now, the model was ready for analysis

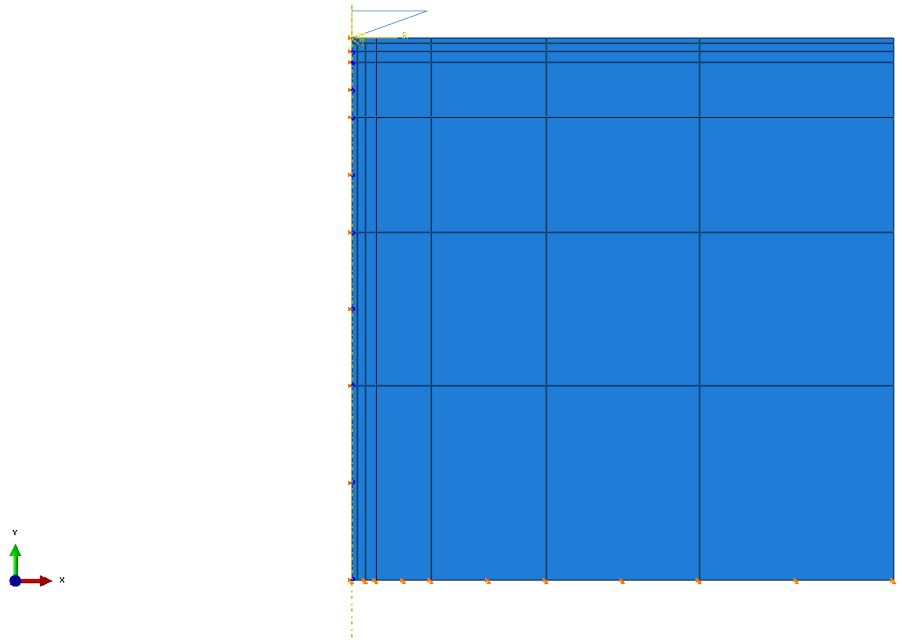

FIGURE 4.7: Boundary conditions

The elastic deformation occurs in the beginning of the process. The mises yield criterion is applied in the occurence of the plastic deformation. The Mises stress criterion is given by the expression

$$\sigma_{Mises} = \sqrt{\frac{(\sigma_1 - \sigma_2)^2 + (\sigma_2 - \sigma_3)^2 + (\sigma_3 - \sigma_1)^2}{2}} \tag{4.1}$$

where σ_1, σ_2, σ_3 are the three principle stresses. When the σ_{Mises} reaches the yield stress of the material(σ_Y), the specimen starts to deform to the plasticity.

4.2 Analysis

After trial and error with the values of modulus and yield stress, load and displacement data that were in the range of the experimental data, were optained. Figure 4.8 shows a typical result.

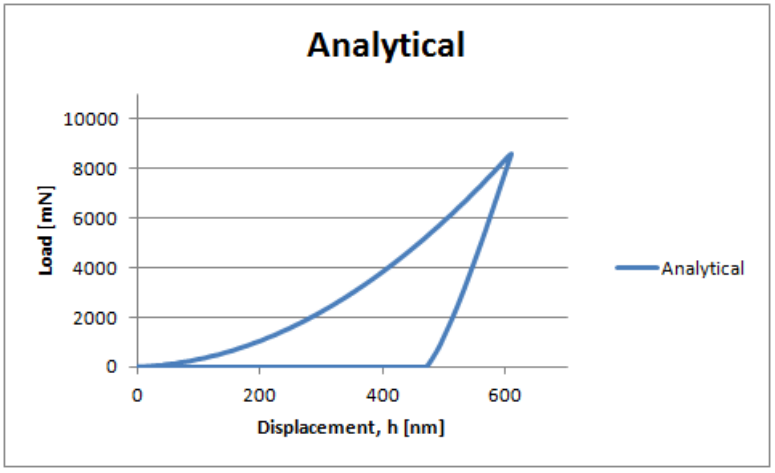

FIGURE 4.8: Illustration of the load-displacement curve after FE analysis. (E = 20 GPa σ_Y = 430 MPa)

Figure 4.9 shows the development of plastic areas as the indenter loads, holds and unloads. Areas with residual stress is noticed after the indenter is completely removed from the bone.

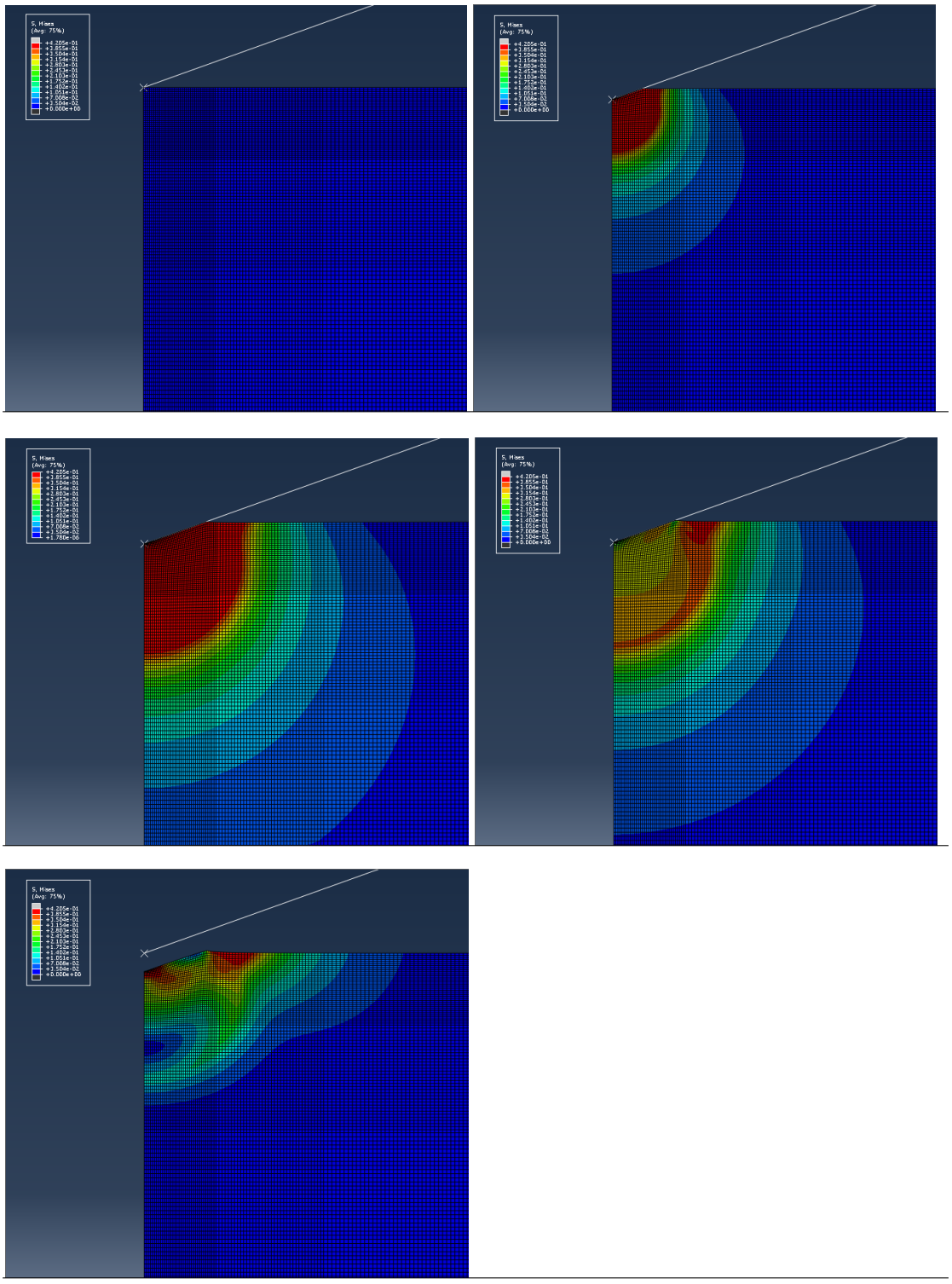

FIGURE 4.9: Analytical indentation from start to hold to finish. Frame 1-2 (top left and right) shows the material response of plastic yield as the load is applied. Frame 3(middle left) shows the indentation at maximum displacement. The plastic yield boundary is seen to stay within a radius from the contact surface. Frame 4-5 (middle right and bottom) shows the unloading part of the indentation. Residual plasticity is located at the initial contact point and at the area outside the indenter contact

In order to inspect how the model acted upon changes in elastic modulus and yield strength, two tests were done. The first one ran many abaqus jobs with different material properties to get an impression on how the response varies. By keeping the modulus at 30 GPa and varying the yield stress, comparisons were made. As the yield drops, the max force increases, and h_c increases, as figure 4.10 shows.

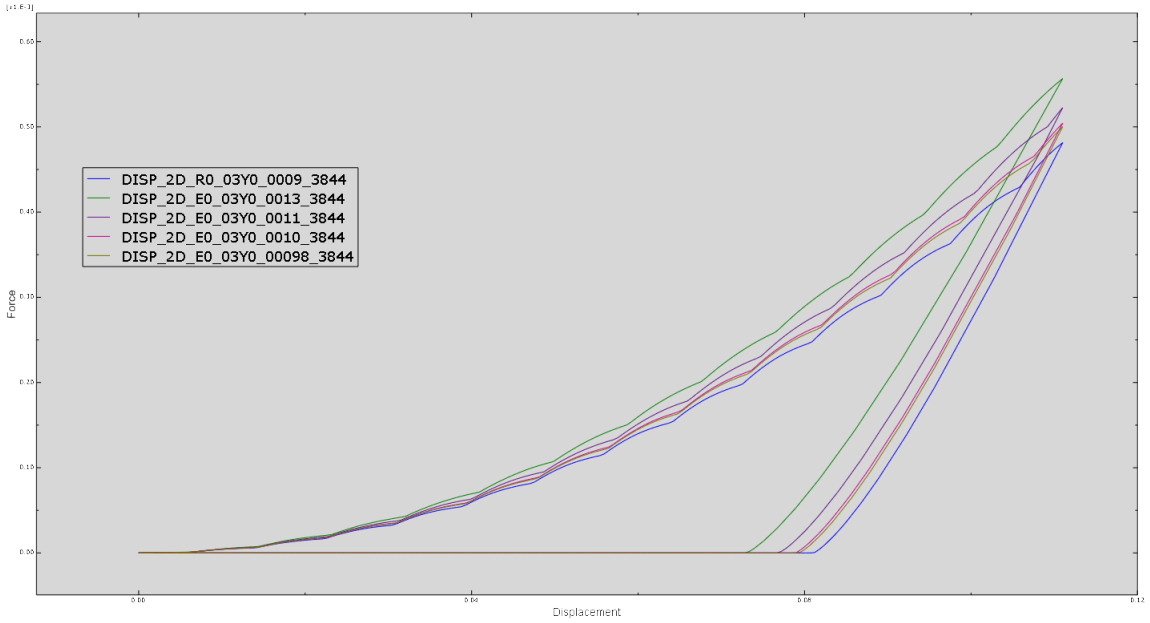

FIGURE 4.10: Constant Young's modulus and varying the yield stress

Now, by varying the elastic modulus, new observations were made. Higher young's modulus resulted in a higher maximum force at the same displacement and higher h_c, as figure 4.11 shows.

The reduced elastic modulus was used to find Young's modulus using equation 2.12 on page 19. The conversion of the results fram sample 1 is shown in table 4.1.

TABLE 4.1: Young's modulus as calculated from the reduced modulus measured by experimental indentation on sample 1. Notice how the difference between reduced modulus and the respective converted Young's modulus grow smaller and smaller as the reduced modulus increase

E/E*$[GPa]$	90 000	90 001	90 002	90 003	90 004	90 005
E*	31,95	35,55	52,58	35,10	94,68	103,22
E	29,92	33,38	50,15	32,94	93,92	103,22

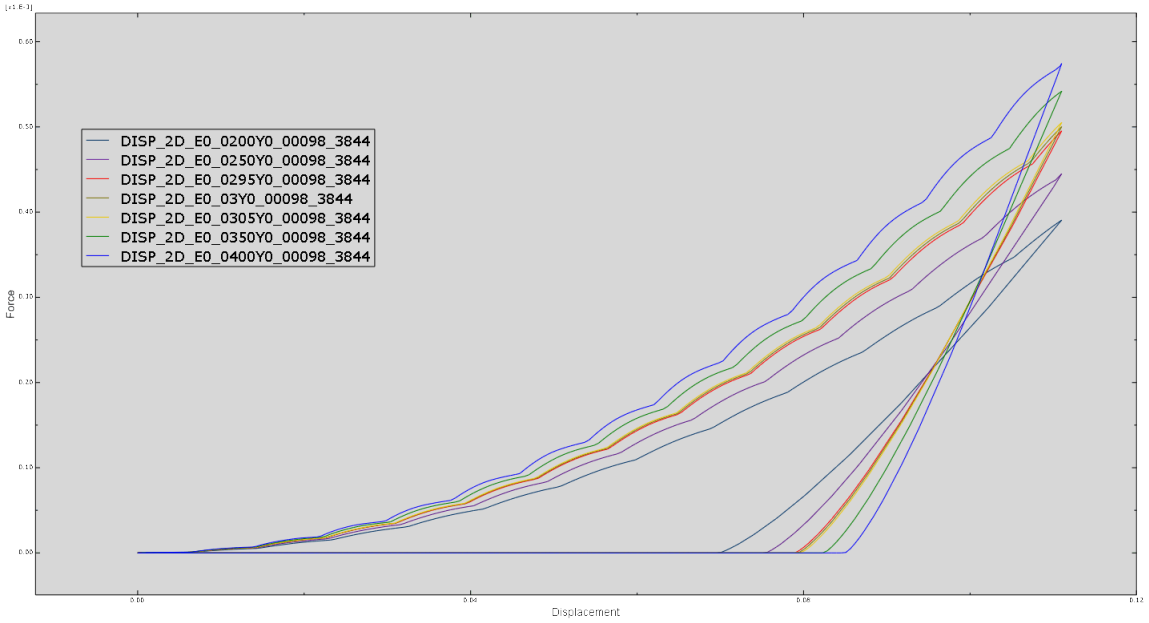

FIGURE 4.11: Constant yield at 98MPa and varying the Young's modulus

4.2.1 Sensitivity to change of E and Yield strength

To investigate how much the model would be affected by a change in elastic modulus and yield strength, three models were compared. One original with elastic modulus of 30GPa and yield stress of 300MPa and the other two with either 10% increased elastic modulus or 10% increased yield strength. Comparing the max load of the two models with the original showed that 10% of increased yield strength would increase the max load with 6,47% while the elastic modulus contributed to an increase of 2,05%. This shows that the model is very sensitive to changes in yield stress - even more than elastic modulus.

4.2.2 Analyzing the model using Oliver and Pharrs procedure

A model was generated using an elastic modulus of 20 GPa and yield strength of 430MPa. Using the unloading curve and the built in curve fitting function in Excel a power function, $P_{unloading}$ (eq. 2.5), was found to be

$21.275(h-\mathrm{h}_f)^{1,2152}$

From here, S was calculated to be $74,722 mN/nm$ and h_c was found to be $516,48 nm$ using the same procedure as presented in chapter 1. As this model uses a cone shaped indenter, the berkovich area funtion is of no use. The area of a cone is given as

$$A(h_c) = \frac{h_c^2 \pi}{cos(70,3)} \tag{4.2}$$

then A(516,48nm) is $2486313,9 nm^2$. Finally, using equation 2.11 E^* was found to be $42,0$ GPa. Using equation 2.12 E was then calculated back to $39,67$ GPa, almost twice the original input value.

This number might be reduced (or increased) when using an imperical factor presented by Oliver and Pharr [15], β. β is a constant that attempts to account for the differences between the azisymmetric contact models and the experimental variations in using pyramidal geometries as well as possible variastions due to plastic deformation, and the fact that the contact area is beyond the small-strain conditions assumes in many conbtact mechanics problems. For Berkovich indenters, the current accepted recommentdation is that using $\beta = 1.034$ or 1.05 will allow reasonably accurate values [12].

Then S is updated to

$$\frac{dP}{dh} = \beta \frac{2}{\sqrt{\pi}} E^* \sqrt{A} \tag{4.3}$$

A value of β should be investigated before claiming the calculated elastic modulus to be too high or too low.

4.2.3 Pile-up

Pile-up [46] was experienced during the analysis as figure 4.12 shows. Piling up and sinking in can be quantifyed by a pile-up parameter given by the ratio of the contact depth h_c over the total depth h_{max} as shown in figure 4.13 [46]

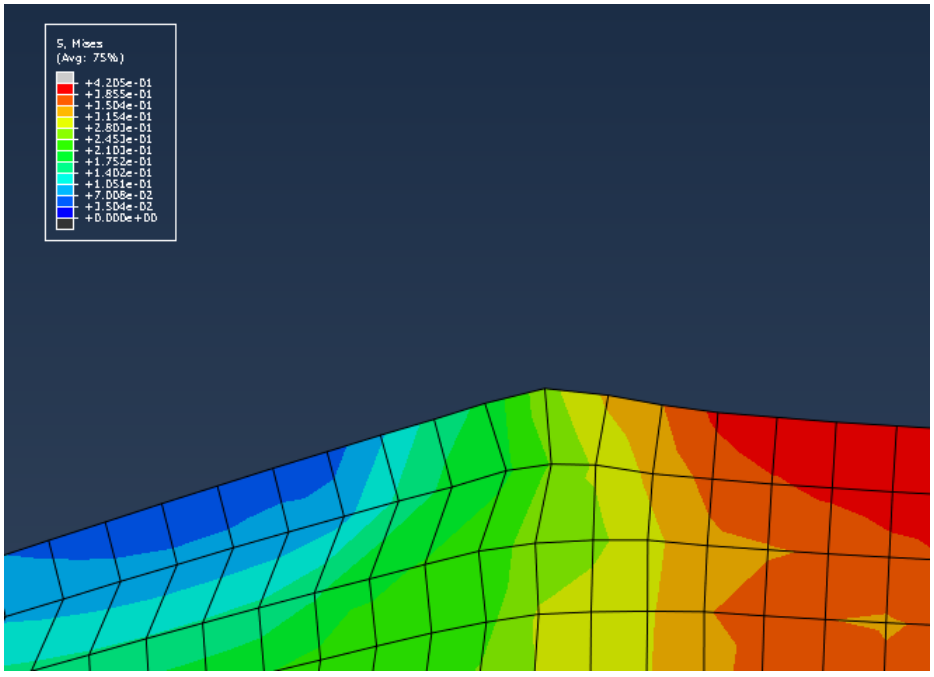

FIGURE 4.12: After the indentation, pile-up is present

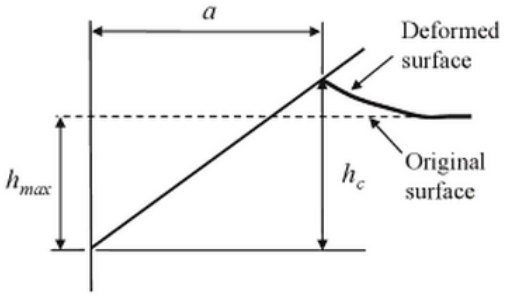

FIGURE 4.13: Pile-up parameter, $\frac{h_c}{h_{max}}$ [46]

The amount of pile up depends on the ratio between E and σ_Y and the amount of strain hardening. For materials with non-strain hardening and with a large value of E/σ_Y , the plastic zone is observed to have a hemispherical shape meeting the surface well outside the radius of the circle of contact. Piling up in these materials

is expected since most of the plastic deformation occurs in the area near of the indenter.

The third image from figure 4.9 (middle left) shows this hemispherical shape as the indenter is at the maximum depth. Also, there is pile-up in the edge, verifying high ratio between E and σ_Y. Finite element testing has been done in an effort to map the influence of pile-up using spherical-conical tips [49]. When using a Berkovich indenter it is considered that a ratio between pile-up and total depht under 0.7 is negligible. Figure 4.9 shows an example where the ratio is calculated to be under 0.1 and therefore the results should not affect any results. They also show that pile-up is a much larger issue when indenting with larger loads(20-80 mN) than has been used in this study(10 mN) and with much greater depths (6000 nm compared to $\approx$ 600 nm in this study).

4.2.4 Discussion

A model has been created with elastic perfect plastic behaviour to simulate the response of experimental indentations of bone samples. Compared to other studies [47] [48] [50] the model behaves similariy, which is comforting.

Pile up was investigated and deemed negligible for the ranges this study operates in. Unfortunatly, there is still a concern to why the calculated modulus using Oliver and Pharrs method differed almost with a factor of 2 when comparing with the input value. The possibility of a β below zero was questioned, but without no certain answer.

Chapter 5

Comparing analytical and experimental results

5.1 Introduction

In chapter 3 and 4 experimental and virtual nanoindentations were done and discussed. To put the finite element model to the test, simulations based on the measured indentation moduli were used in the model, creating load-displacement curves that could be compared with the experiment.

Based on the poor results from sample 1, it was discarded. In order to match the load-unload curves as accuratly as possible with a given indentation modulus, an iterating process, consisting of changing the σ_Y until the max load approached 10mN, was done. As a result of long simulation time (two hours per analysis), and the need for many iterations, the results from sample 2 were discarded along with half of the results from sample 3, leaving six indentations from sample 3.

It was concluded to only accuratly estimate the σ_Y of one indentation and to use this value when running the five other simulations. Figure shows the simulated results with the experimental results.

For these six indentations, the model was compared to the experimental results of sample 3. The yield was kept constant at 421 MPa. This resulted in varying max loads, as figure 3 shows. This shows how dependent the model is of the plastic yield strength, as previously shown in chapter 4, section 4.2.1 on page 57.

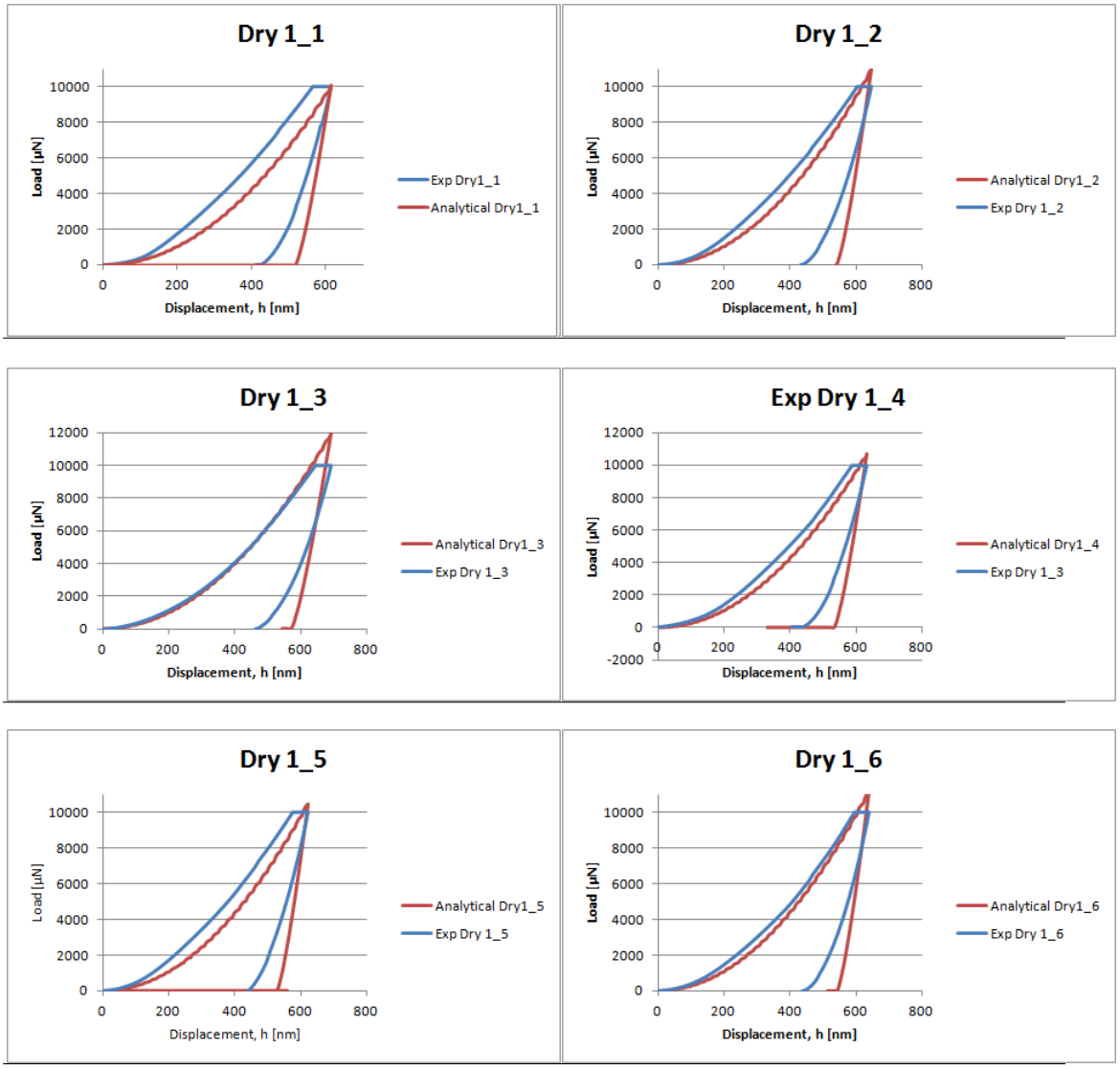

FIGURE 5.1: Six experimental indentations from sample 3 were compared to the analytical results using the same elastic moduli extracted from the tests. The yield strength was set to 421 MPa for all tests.

5.1.1 Discussion

The elastic perfectly plastic model shows significant resemblence to the experimental results. Still, the unloading curves do not match when the same elastic

modulus is used for both the experimental indentation and equivalent analytical indentation. This misfit seems to be accepted in the literature [48] [50]. The curves should be expected to misalign since bone, as previously stated, is in fact not elastic perfect plast, but visco elastic damage plastic. Even though an acute indenter, such as the Berkovich, was applied, there is still visco elastic influence on the unloading curve [29].

It has also been shown that an elastic perfect plastic model overestimates the max load with 10% [48]. A question was raised: Perhaps the tangent at maxload was identical for the analytical and experimental data, and viscoelastic behaviour was distorting the alignment. It was easy to check this by matching the tangents at max load. Unfortunatly, they did not match. As an attempt to match the unloading curves, the elastic modulus was changed until the unloading curves matched. This was done through trial and error. For instance, indentation 4, sample 3, was experimentally reported to have an elastic moduli of 32,45 GPa. However, the finite element model needed a modulus of 20 GPa to match the curve. The match is shown at figure 5.2

This shows that it is possible to use the model to reverse engineer the yield strength and elastic modulus of mouse femur. Is it likely the extracted values are correct? No. C.H. Turner et al. [51] reported of ultimate compressive strength of 135MPa, from a tensile compression test on human femur at mesoscale, which is expected to be at least larger than the yield stress, estimated to be $\approx$ 600MPa in this study. Therefore, it would be better to improve the model by adding visco-elastic properties and damage plastic hardening to the material property. It should also be mentioned, that the experimental testing and analysis protocol is intended on elastic plastic materials, not visco elastic materials such as bone. Therefore, the calculated reduced moduli might also be off [29].

In addition, the pile up around the experimental indentations was not investigated and could therefore not be compared to the analytical. Even though pile up has been tested to be non significant on low depths [49] these were done on an

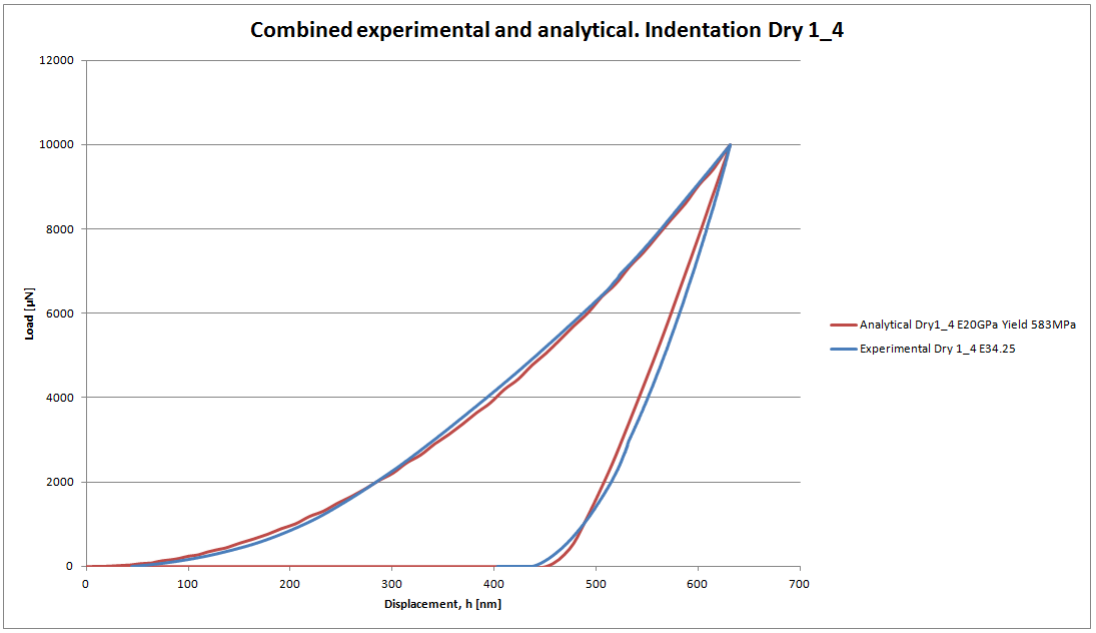

FIGURE 5.2: Overlaying analytical and experimental load-displacement curves. The experimental curve has a reported elastic modulus of 34,25GPa. To resemble this curve with the elastic perfectly plastic model, a modulus of 20GPa and σ_Y of 583MPa has been chosen. Also, the holding time has been removed from the experimental curve, and the loading part shifted to match the analytical curve

aluminium cobber alloy, which does not directly translate to a viscoelastic plastic material, such as bone.

In conclusion, the experimental tests have shown to be fairly coherent with other studies, and suggestions to an improved protocol has been made in order to increase the accuracy of the testing. The analytical model has also been shown to display many similar features to the experimental data, such as a curved load and an unloading curve that follows the power law function (equation 2.5 on page 17). In order to match the curves, very high yield strength was needed (400-600 MPa) with a much lower elastic modulus than calculated from the experimental tests. It is advised to rather improve the model further by adding damage plastic model [48] and experimenting with viscoelastic behaviour before reverse engineering should be trusted.

Chapter 6

Conclusion and future work

6.1 Conclusion

Using nanoindentation as a tool for measurement of material properties is becoming more and more popular. Even though there are hundreds, if not thousands, of studies on nanoindentation in the field of biomechanics, the mechanics of bone has not yet been understood in a satisfactory degree. This study has compared experimental testing of mice femur to analytical testing in the commercial FEM software, Abaqus. Dispite poor testing protocol and an oversimplyfied FE model, the results have showed promising behaviour. It has been shown that it is in fact possible to obtain the material properties of the mice femur through reverse engineering, but the extracted properties should be handled with care, as they differ greatly from the experimental tests and other studies. It has also been seen that the experimental results are promising, but the protocol has much room for improvement.

On this basis, suggestions on improvements have been made for both the experimental testing protocol and the material properties in the analytical model.

6.2 Future work

The model presented in this thesis has proved to not describe the indented bone on a satisfactory level. Therefore it is considered a bottleneck for the validity of future FE studies. As this project's main goal is to compare healthy to sick bones, the experimental protocol should be addressed and improved as previously suggested. When using a Berkovich pyramid, the material is almost guaranteed to get plastically deformed. By using Oliver and Pharr's method, the errors might be very large if the viscosity of the material is not taken into account [29]

Suggestions for future work regarding general improvement of understanding bone mechanics are:

- Adding damage plastic properties to the model, as suggested by Paruchuru et al. [48]
- Adding visco elastic properties as described by Oyen et al. [29] [24]
- Experimenting with anisotropic properties as mention in chapter 2 [34] [52] [53]. It might be necessary to alter the experimental protocol so that it includes anisotropic testing.
- Atomic Force Measurement(AFM) has been meantioned in the literature [41] [21] as a tool proven to be powerful combine with the nanoindenter to characterize single bone lamellae under dry and physiological conditions and should be investigated as a possible tool in future work.
- Scripting the analysis process in Abaqus and Matlab: Creating a script that submits Abaqus jobs and extracts the proper information. This information should be automatically processed by, for instance, Matlab to output all analysis. This way, parameter fitting is greatly improved in effectiveness.

When the model accuracy is satisfied, the next step should involve comparing mechanical features on the micro and macroscopical levels. There have been attempts

on creating a link between macroscopic measurements and nanoindentation [54] where it is concluded that the relationships between micro- and macroscopic levels are not well understood. An interesting way to attempt building a bridge between the two levels is by creating a computer tomography scan of the bone [55]. It is a medical imaging method that employs tomography. Tomography is the process of generating a two-dimensional image of a slice or section through a 3-dimensional object (a tomogram). It is possible to use a computed tomography scanner to build a finite element model of biological materials. By assigning each pixel a density, a volume based 3D voxel model can be created(figure 6.1).

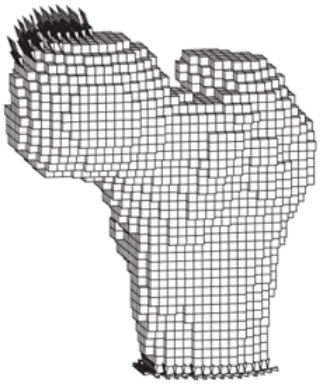

FIGURE 6.1: Example of voxel based CT scan taken from [56]

This way, it is possible to replicate the excact experimental indentations in Abaqus and fit the parameters accordingly. This is predicted to be immensely tedious work and the analysis jobs should be scripted.

These are just some of the areas that need to be examined, but they all require an extensive amount of work.

Appendix A

Sample input file

*Heading

** Job name: $\mathrm{Dry1}_2\mathrm{0}Modelname : 10mN_200x200 - Dry_{16}31_46E20$

$* *Generatedby : Abaqus/CAE6.11 - 1$

$* Preprint, echo = NO, model = NO, history = NO, contact = NO$

* *

$* *PARTS$

* *

$* Part, name = "Indenter10[um]"$

$* EndPart$

* *

$* Part, name = "Plate200X200[um2]"$

$* Node$

$1, 128.279999, -128.279999$

$2, 128.279999, -200.$

(...)

60024,	60515,	60516,	3770,	3769
60025,	60516,	3771,	58,	3770

*Nset, nset=$_P ickedSet6, internal, generate$

$1, 60516, 1$

$* Elset, elset =_P ickedSet6, internal, generate$

1, 60025, 1

∗ ∗*Section* : *BoneEpP*

∗ *SolidSection*, *elset* =$_P$ *ickedSet*6, *material* = ”*BEP*”

,

∗ *EndPart*

∗ ∗

∗ ∗

∗ ∗*ASSEMBLY*

∗ ∗

∗ *Assembly*, *name* = *Assembly*

∗ ∗

∗ *Instance*, *name* = ”*Plate*200*X*200[*um*2] − 1”, *part* = ”*Plate*200*X*200[*um*2]”

∗ *EndInstance*

∗ ∗

∗ *Instance*, *name* = ”*Indenter*10[*um*] − 1”, *part* = ”*Indenter*10[*um*]”

∗ *Node*

1, 0., 4.4408921*e* − 16, 0.

∗ *Nset*, *nset* = ”*Indenter*10[*um*] − 1 − *RefPt*», *internal*

1,

∗ *Surface*, *type* = *SEGMENTS*, *name* = ”*Indenter*1”

START, 0., 10.

LINE, 27.9289168651081, 10.

LINE, 0., 0.

∗ *EndInstance*

∗ ∗

∗ *Nset*, *nset* = ”*RefIndent*1”, *instance* = ”*Indenter*10[*um*] − 1”

1,

∗ *Nset*, *nset* = *Bot*, *instance* = ”*Plate*200*X*200[*um*2] − 1”

2, 3, 8, 13, 19, 30, 33, 34, 99, 100, 101, 102, 103, 104, 105, 106

(...)

2185, 2186, 2187, 2188, 2189, 2190, 2191, 2192, 2193, 2194, 2195, 2196, 2197, 2198, 2199, 2200

2201, 2202, 2203, 2204, 2205, 2206

∗ *Elset*, *elset* = *Bot*, *instance* = ”*Plate*200*X*200[*um*2] − 1”

35, 70, 105, 140, 175, 210, 245, 280, 315, 350, 385, 420, 455, 490, 525, 560

(...)

28666, 28701, 28736, 28771, 28806, 28841, 28876, 28911, 28946, 28981, 29016, 29051, 29086, 29121, 29156, 29191

29226, 29261, 29296, 29331, 29366

∗ *Nset*, *nset* = *Center*, *instance* = ”*Plate*200*X*200[*um*2] − 1”

$32, 33, 42, 49, 55, 61, 62, 64, 1595, 1596, 1597, 1598, 1599, 1600, 1601, 1602$

(...)

$3851, 3852, 3853, 3854, 3855, 3856, 3857, 3858, 3859, 3860, 3861, 3862, 3863, 3864, 3865, 3866$

$3867, 3868, 3869, 3870, 3871, 3872$

$*\, Elset, elset = Center, instance = "Plate200X200[um2] - 1"$

$19635, 19670, 19705, 19740, 19775, 19810, 19845, 19880, 19915, 19950, 19985, 20020, 20055, 20090, 20125, 20160$

(...)

$58066, 58101, 58136, 58171, 58206, 58241, 58276, 58311, 58346, 58381, 58416, 58451, 58486, 58521, 58556, 58591$

$58626, 58661, 58696, 58731, 58766$

$*\, Elset, elset = "_{T}opPlate1_{S}4", internal, instance = "Plate200X200[um2] - 1", generate$

$12251, 13441, 35$

$*\, Elset, elset = "_{T}opPlate1_{S}2", internal, instance = "Plate200X200[um2] - 1"$

$20860, 20895, 20930, 20965, 21000, 21035, 21070, 21105, 21140, 21175, 21210, 21245, 21280, 21315, 21350, 21385$

(...)

$54530, 54565, 54600, 54635, 54670, 54705, 54740, 54775, 54810, 54845, 54880, 54915, 54950, 54985, 55020, 55055$

$55090, 55125$

$*\, Surface, type = ELEMENT, name = "TopPlate1"$

$"_{T}opPlate1_{S}4", S4$

$"_{T}opPlate1_{S}2", S2$

$*\, Elset, elset = "_{B}otPlate1_{S}2", internal, instance = "Plate200X200[um2] - 1", generate$

$35, 1225, 35$

$*\, Elset, elset = "_{B}otPlate1_{S}4", internal, instance = "Plate200X200[um2] - 1"$

$2451, 2486, 2521, 2556, 2591, 2626, 2661, 2696, 2731, 2766, 2801, 2836, 2871, 2906, 2941, 2976$

(...)

$28876, 28911, 28946, 28981, 29016, 29051, 29086, 29121, 29156, 29191, 29226, 29261, 29296, 29331, 29366$

$*\, Elset, elset = "_{B}otPlate1_{S}3", internal, instance = "Plate200X200[um2] - 1", generate$

$20791, 20825, 1$

$*\, Surface, type = ELEMENT, name = "BotPlate1"$

$"_{B}otPlate1_{S}2", S2$

$"_{B}otPlate1_{S}4", S4$

$"_{B}otPlate1_{S}3", S3$

$**Constraint : Indent1Rigid$

$*RigidBody, refnode = "RefIndent1", analyticalsurface = "Indenter10[um]-1"."Indenter1"$

$*\, EndAssembly$

$**$

$**MATERIALS$

$**$

$*\, Material, name = "BEP"$

$*Elastic$

$20., 0.3$

$*Plastic$

$0.43, 0.$

$**$

$**INTERACTIONPROPERTIES$

$**$

$*SurfaceInteraction, name = noFric$

$1.,$

$*Friction$

$0.,$

$**$

$**BOUNDARYCONDITIONS$

$**$

$**Name : BotType : Displacement/Rotation$

$*Boundary$

$Bot, 1, 1$

$Bot, 2, 2$

$**Name : CenterType : Displacement/Rotation$

$*Boundary$

$Center, 1, 1$

$Center, 6, 6$

$**Name : IndRU3Type : Displacement/Rotation$

$*Boundary$

$"RefIndent1", 6, 6$

$**Name : IndU1Type : Displacement/Rotation$

$*Boundary$

$"RefIndent1", 1, 1$

$**$

$**INTERACTIONS$

$**$

$**Interaction : Interaction$

$*ContactPair, interaction = noFric$

$"TopPlate1","Indenter10[um] - 1"."Indenter1"$

$**----------$

$----------$

$**$

$**STEP : Step - 1$

$**$

$*Step, name = Step - 1, nlgeom = YES, inc = 1000$

$*Static$

$0.0015, 1., 1e - 12, 1.$

$**$

$**BOUNDARY CONDITIONS$

$**$

$**Name : IndU2Type : Displacement/Rotation$

$*Boundary$

$"RefIndent1", 2, 2, -0.63146$

$**$

$**INTERACTIONS$

$**$

$**ContactControls for Interaction : Interaction$

$*ContactControls, master = "Indenter10[um] - 1"."Indenter1", slave = "TopPlate1", reset$

$*ContactControls, master = "Indenter10[um]-1"."Indenter1", slave = "TopPlate1", stabilize = 0.001$

$**$

$**OUTPUT REQUESTS$

$**$

$*Restart, write, frequency = 0$

$**$

$**FIELD OUTPUT : F - Output - 1$

$**$

$*Output, field, variable = PRESELECT$

$**$

$**HISTORY OUTPUT : H - Output - 1$

$**$

$*Output, history, variable = PRESELECT$

$*EndStep$

$**----------$

$**$

$**STEP : Step - 3$

$**$

$*Step, name = Step - 3, nlgeom = YES, inc = 1000$

$*Static$

$0.001, 1., 1e - 12, 1.$

$**$

$**OUTPUTREQUESTS$

$**$

$*Restart, write, frequency = 0$

$**$

$**FIELDOUTPUT : F - Output - 1$

$**$

$*Output, field, variable = PRESELECT$

$**$

$**HISTORYOUTPUT : H - Output - 1$

$**$

$*Output, history, variable = PRESELECT$

$*EndStep$

$**----------$

$----------$

$**$

$**STEP : Step - 2$

$**$

$*Step, name = Step - 2, nlgeom = YES, inc = 1000$

$*Static$

$0.0015, 1., 1e - 12, 1.$

$**$

$**BOUNDARYCONDITIONS$

$**$

$**Name : BotType : Displacement/Rotation$

$*Boundary, op = NEW$

$Bot, 1, 1$

$Bot, 2, 2$

$**Name : CenterType : Displacement/Rotation$

$*Boundary, op = NEW$

$Center, 1, 1$

$Center, 6, 6$

$**Name : IndRU3Type : Displacement/Rotation$

$*Boundary, op = NEW$

$"RefIndent1", 6, 6$

$**Name : IndU1Type : Displacement/Rotation$

$*Boundary, op = NEW$

$"RefIndent1", 1, 1$

$**Name : IndU2Type : Displacement/Rotation$

$*Boundary, op = NEW$

$**Name : IndU2retractType : Displacement/Rotation$

$*Boundary, op = NEW$

"$RefIndent1$", $2, 2$

$**$

$**OUTPUTREQUESTS$

$**$

$*Restart, write, frequency = 0$

$**$

$**FIELDOUTPUT : F - Output - 1$

$**$

$*Output, field, variable = PRESELECT$

$**$

$**HISTORYOUTPUT : H - Output - 1$

$**$

$*Output, history, variable = PRESELECT$

$*EndStep$

Bibliography

[1] MD Gustava de la Roza, MD;Chief Editor: Harris Gellman. Histology of bone.

[2] PhD Bejamin McVay Petre, MD; Chief Editor: Thomas R Gest. Osteology(bone anatomy.

[3] JohnD Currey. The structure and mechanics of bone. *Journal of Materials Science*, 47(1):41–54, 2012.

[4] Jae-Young Rho, Liisa Kuhn-Spearing, and Peter Zioupos. Mechanical properties and the hierarchical structure of bone. *Medical Engineering Physics*, 20(2):92–102, 1998.

[5] June 2013. URL http://kids.britannica.com/comptons/art-126587/A-longitudinal-section-seen-from-the-front-shows-the-various.

[6] June 2013. URL http://www.proprofs.com/quiz-school/story.php?title=anatomy-and-physiology-questions-the-skeletal-system-bone-tissue.

[7] October 2012. URL http://medcell.med.yale.edu/histology_old/bone/images/bone_structure_cartoon.jpg.

[8] K. L. Johnson. Contact mechanics. pages 84–106.

[9] June 2013. URL http://courses.washington.edu/overney/ChemE554_Course_Mat/course_material/Ch_2_Contact%20Mechanics.pdf.

[10] June 2013. URL http://www.instron.us/wa/applications/test_types/hardness/rockwell.aspx.

[11] Ian M. Hutchings. The contributions of david tabor to the science of indentation hardness. *Journal of Materials Research*, 24(03):581–589, 2009.

[12] DavidF Bahr and DylanJ Morris. *Nanoindentation: Localized Probes of Mechanical Behavior of Materials*, chapter 16, pages 389–408. Springer US, 2008.

[13] M.F. Doerner and W.D. Nix. A method for interpreting the data from depth-sensing indentation instruments. *Journal of Materials Research*, 1(04):601–609, 1986.

[14] W.C. Oliver and G.M. Pharr. An improved technique for determining hardness and elastic modulus using load and displacement sensing indentation experiments. *Journal of Materials Research*, 7(06):1564–1583, 1992.

[15] W.C. Oliver and G.M. Pharr. Measurement of hardness and elastic modulus by instrumented indentation: Advances in understanding and refinements to methodology. *Journal of Materials Research*, 19(01):3–20, 2004.

[16] June 2013. URL http://www.engineering.unl.edu/research/bm3/graphics/nanoindenter_Berkovich_tip_01.jpg.

[17] June 2013. URL http://www.hysitron.com/Portals/0/Technique%20Images/nanoindentation01.png.

[18] June 2013. URL http://www.charfac.umn.edu/pictures/triboindenter2.jpg.

[19] June 2013. URL http://www.hysitron.com/Portals/0/ProductImages/afm_imaging_horizontal.jpg.

[20] S. V. Hainsworth, H. W. Chandler, and T. F. Page. Analysis of nanoindentation load-displacement loading curves. *Journal of Materials Research*, 11 (08):1987–1995, 1996.

[21] Donna M. Ebenstein and Lisa A. Pruitt. Nanoindentation of biological materials. *Nano Today*, 1(3):26–33, 2006.

[22] David P. Fyhrie. Zheng wu et al.: the effect of holding time on nanoindentation measurements of creep in bone [j. biomech. 44 (2011) 10661072]. *Journal of Biomechanics*, 44(13):2520, 2011.

[23] Tara N. Shepherd, Jingzhou Zhang, Timothy C. Ovaert, Ryan K. Roeder, and Glen L. Niebur. Direct comparison of nanoindentation and macroscopic measurements of bone viscoelasticity. *Journal of the Mechanical Behavior of Biomedical Materials*, 4(8):2055–2062, 2011.

[24] Michelle L. Oyen and Robert F. Cook. A practical guide for analysis of nanoindentation data. *Journal of the Mechanical Behavior of Biomedical Materials*, 2(4):396–407, 2009.

[25] Michelle L. Oyen. Spherical indentation creep following ramp loading. *Journal of Materials Research*, 20(08):2094–2100, 2005.

[26] Naiara Rodriguez, Michelle L. Oyen, and Sandra J. Shefelbine. Insight into differences in nanoindentation properties of bone. *Journal of the Mechanical Behavior of Biomedical Materials*, (0).

[27] June 2013. URL http://www.sciencedirect.com/science/article/pii/S0300944003001450.

[28] S. Pathak, S. J. Vachhani, K. J. Jepsen, H. M. Goldman, and S. R. Kalidindi. Assessment of lamellar level properties in mouse bone utilizing a novel spherical nanoindentation data analysis method. *J Mech Behav Biomed Mater*, 13C:102–117, 2012.

[29] SaraE Olesiak, MichelleL Oyen, and VirginiaL Ferguson. Viscous-elastic-plastic behavior of bone using berkovich nanoindentation. *Mechanics of Time-Dependent Materials*, 14(2):111–124, 2010.

[30] Jae-Young Rho, Ting Y. Tsui, and George M. Pharr. Elastic properties of human cortical and trabecular lamellar bone measured by nanoindentation. *Biomaterials*, 18(20):1325–1330, 1997.

[31] Anna Faingold, Sidney R. Cohen, and H. Daniel Wagner. Nanoindentation of osteonal bone lamellae. *Journal of the Mechanical Behavior of Biomedical Materials*, 9(0):198–206, 2012.

[32] J. Y. Rho, P. Zioupos, J. D. Currey, and G. M. Pharr. Variations in the individual thick lamellar properties within osteons by nanoindentation. *Bone*, 25(3):295–300, 1999.

[33] Z. Fan, J. G. Swadener, J. Y. Rho, M. E. Roy, and G. M. Pharr. Anisotropic properties of human tibial cortical bone as measured by nanoindentation. *Journal of Orthopaedic Research*, 20(4):806–810, 2002.

[34] Andreas G. Reisinger, Dieter H. Pahr, and Philippe K. Zysset. Principal stiffness orientation and degree of anisotropy of human osteons based on nanoindentation in three distinct planes. *Journal of the Mechanical Behavior of Biomedical Materials*, 4(8):2113–2127, 2011.

[35] T. Hoc, L. Henry, M. Verdier, D. Aubry, L. Sedel, and A. Meunier. Effect of microstructure on the mechanical properties of haversian cortical bone. *Bone*, 38(4):466–474, 2006.

[36] Michelle L. Oyen, Virginia L. Ferguson, Amanpreet K. Bembey, Andrew J. Bushby, and Alan Boyde. Composite bounds on the elastic modulus of bone. *Journal of Biomechanics*, 41(11):2585–2588, 2008.

[37] Philippe K. Zysset, X. Edward Guo, C. Edward Hoffler, Kristin E. Moore, and Steven A. Goldstein. Elastic modulus and hardness of cortical and trabecular bone lamellae measured by nanoindentation in the human femur. *Journal of Biomechanics*, 32(10):1005–1012, 1999.

[38] Rho J-Y. and Pharr G.M. Effects of drying on the mechanical properties of bovine femur measured by nanoindentation. *Journal of Materials Science: Materials in Medicine*, 10(8):485–488, 1999. URL http://www.ingentaconnect.com/content/klu/jmsm/1999/00000010/00000008/00234508.

[39] C. Edward Hoffler, X. Edward Guo, Philippe K. Zysset, and Steven A. Goldstein. An application of nanoindentation technique to measure bone tissue lamellae properties. *Journal of Biomechanical Engineering*, 127(7):1046–1053, 2005.

[40] P. K. Zysset. Indentation of bone tissue: a short review. *Osteoporosis International*, 20(6):1049–1055, 2009.

[41] S. Hengsberger, A. Kulik, and Ph Zysset. Nanoindentation discriminates the elastic properties of individual human bone lamellae under dry and physiological conditions. *Bone*, 30(1):178–184, 2002.

[42] Jae-Young Rho, Marcel E. Roy, Ting Y. Tsui, and George M. Pharr. Elastic properties of microstructural components of human bone tissue as measured by nanoindentation. *Journal of Biomedical Materials Research*, 45(1): 48–54, 1999. ISSN 1097-4636. doi: 10.1002/(SICI)1097-4636(199904)45:1⟨48::AID-JBM7⟩3.0.CO;2-5. URL http://dx.doi.org/10.1002/(SICI)1097-4636(199904)45:1<48::AID-JBM7>3.0.CO;2-5.

[43] C. E. Hoffler, K. E. Moore, K. Kozloff, P. K. Zysset, M. B. Brown, and S. A. Goldstein. Heterogeneity of bone lamellar-level elastic moduli. *Bone*, 26(6): 603–609, 2000.

[44] Siddhartha Pathak, J. Gregory Swadener, Surya R. Kalidindi, Hayden-William Courtland, Karl J. Jepsen, and Haviva M. Goldman. Measuring the dynamic mechanical response of hydrated mouse bone by nanoindentation. *Journal of The Mechanical Behavior of Biomedical Materials*, 4:34–43, 2011. doi: 10.1016/j.jmbbm.2010.09.002.

[45] Kevin M. Middleton, Beth D. Goldstein, Pradeep R. Guduru, Julie F. Waters, Scott A. Kelly, Sharon M. Swartz, and T. Garland Jr. Variation in within-bone stiffness measured by nanoindentation in mice bred for high levels of voluntary wheel running. *Journal of Anatomy*, 216(1):121–131, 2010. ISSN 1469-7580. doi: 10.1111/j.1469-7580.2009.01175.x. URL http://dx.doi.org/10.1111/j.1469-7580.2009.01175.x.

[46] Anthony C. Fischer-Cripps. Nanoindentation. pages 88–91, 2011. ISSN 0941-5122. doi: 10.1007/978-1-4419-9872-9. URL http://books.google.no/books?id=D23TpyBM_EcC&printsec=frontcover&hl=no&source=gbs_ge_summary_r&cad=0#v=onepage&q=pile-up&f=false.

[47] K K Tho S Swaddiwudhipong, J Hua and Z S Liu. Equivalency of berkovich and conical load-indentation curves. *Modelling Simul. Mater. Sci. Eng.*, 14 (1):71, 2006. URL http://stacks.iop.org/0965-0393/14/i=1/a=006.

[48] Satya Prasad Paruchuru, Xiaodu Wang, and Xuanliang Dong. Finite element simulation of nanoindentation tests for cortical bone using a damage plastic model. *Strength, Fracture and Complexity*, 6(3):83–89, 2010.

[49] M.A. Garrido Maneiro and J. Rodrguez. Pile-up effect on nanoindentation tests with sphericalconical tips. *Scripta Materialia*, pages 593 – 598, 2005. ISSN 1359-6462. doi: 10.1007/978-1-4419-9872-9. URL http://www.sciencedirect.com/science/article/pii/S135964620400675X.

[50] Nanoindentation of silicon (100) studied by experimental and finite element method. *Scripta Materialia*, 2003.

[51] C.H. Turner and D.B. Burr. Basic biomechanical measurements of bone: A tutorial. *Bone*, 14(4):595 – 608, 1993. ISSN 8756-3282. doi: 10.1016/8756-3282(93)90081-K. URL http://www.sciencedirect.com/science/article/pii/875632829390081K.

[52] Davide Carnelli, Riccardo Lucchini, Matteo Ponzoni, Roberto Contro, and Pasquale Vena. Nanoindentation testing and finite element simulations of cortical bone allowing for anisotropic elastic and inelastic mechanical response. *Journal of Biomechanics*, 44(10):1852–1858, 2011.

[53] Z. Fan, J. G. Swadener, J. Y. Rho, M. E. Roy, and G. M. Pharr. Anisotropic properties of human tibial cortical bone as measured by nanoindentation. *Journal of Orthopaedic Research*, 20(4):806–810, 2002. ISSN 1554-527X. doi: 10.1016/S0736-0266(01)00186-3. URL http://dx.doi.org/10.1016/S0736-0266(01)00186-3.

[54] Tara N. Shepherd, Jingzhou Zhang, Timothy C. Ovaert, Ryan K. Roeder, and Glen L. Niebur. Direct comparison of nanoindentation and macroscopic measurements of bone viscoelasticity. *Journal of the Mechanical Behavior of Biomedical Materials*, 4(8):2055 – 2062, 2011. ISSN 1751-6161. doi: 10.1016/j.jmbbm.2011.07.004. URL http://www.sciencedirect.com/science/article/pii/S1751616111001913. ¡ce:title¿Special Issue Soft Tissues¡/ce:title¿ ¡ce:subtitle¿Special Issue Section on Soft Tissue 3d Strain¡/ce:subtitle¿.

[55] Yan Chevalier. Computer tomography-based finite element analysis of the human vertebral body. 2008.

[56] J. H. Keyak. Improved prediction of proximal femoral fracture load using nonlinear finite element models. *Medical Engineering Physics*, 23(3):165–173, 2001.